# Physicochemical aspects of magnetite gabbro formation in the layered intrusion of the Western Pansky Tundra, Kola Peninsula, Russia

**Article** *in* Petrology · January 2001

CITATIONS
5

READS
104

**2 authors:**

Rais Latypov
University of the Witwatersrand
**107** PUBLICATIONS **1,012** CITATIONS
SEE PROFILE

Sofia Chistyakova
University of the Witwatersrand
**48** PUBLICATIONS **371** CITATIONS
SEE PROFILE

*Petrology, Vol. 9, No. 1, 2001, pp. 25–45. Translated from Petrologiya, Vol. 9, No. 1, 2001, pp. 28–50.*


# Physicochemical Aspects of Magnetite Gabbro Formation in the Layered Intrusion of the Western Pansky Tundra, Kola Peninsula, Russia

**R. M. Latypov[1] and S. Yu. Chistyakova**

*Geological Institute, Kola Research Center, Russian Academy of Sciences,*
*ul. Fersmana 14, Apatity, Murmanskaya oblast, 184200 Russia*
*e-mail: lat@geo.kolasc.net.ru*

Received February 12, 2000

**Abstract**—Magnetite gabbro occurs in the central part of the layered intrusion of the western Pansky Tundra as layers and lenticular bodies from 20 to 100 m thick and from hundreds of meters to 10 km long. They show fine-grained textures and contain cumulus magnetite, iron-rich pyroxenes, and low-calcium plagioclase. The transition from the enclosing gabbronorite (*Pl–Cpx–Opx* cumulate) through gabbronorite with inverted pigeonite (*Pl–Cpx–Opx–Pig#* cumulate) to the magnetite gabbro bodies with inverted pigeonite (*Pl–Cpx–Opx–Pig#–Mgt* cumulate) is accompanied by successive appearance of new cumulus phases, pigeonite and magnetite (phase layering); gradual increase of clinopyroxene fraction on the expense of orthopyroxene (modal layering); regular increase in the iron content of pyroxene; and decrease in the anorthite content of plagioclase (cryptic layering). These observations allow us to interpret the magnetite gabbro with inverted pigeonite as the final product of the Fenner trend of chamber differentiation of the initial melt of the Western Pansky Tundra intrusion. It is assumed that during intrusion consolidation, the residual melt portions were concentrated in isolated subchambers elongated in accord with the general structural plan of the massif. The opposing walls of the subchambers converged gradually during crystallization, and fluid pressure increased continuously, while the composition of liquid changed and its volume decreased. Tectonic movements and (or) high fluid pressure resulted in wall fracturing and fluid loss from the subchambers. This brought the melt into a state of strong oversaturation and caused its rapid crystallization and formation of fine-grained magnetite gabbro depleted in incompatible elements, which were removed from the system by the fluid phase.

## INTRODUCTION

The nature of magnetite gabbro bodies is one of the main problems in the petrology of the layered intrusion of the Western Pansky Tundra, because it is crucial for understanding the mechanism of massif differentiation. The complexity of the problem is related to the fact that, on the one hand, the gradual transition to the enclosing gabbronorite suggests that the magnetite gabbro is inherent part of the intrusion section. On the other hand, some features of the magnetite gabbro including its occurrence at various stratigraphic levels of the intrusion section, fine-grained texture, and highly evolved composition are distinctly different from most of the gabbronorite that compose the intrusion. Thus, an independent origin of these rocks different from that of the gabbronorite can be assumed. This resulted in the emergence of contradictory hypotheses on the magnetite gabbro genesis. The magnetite gabbro is considered as either syngenetic rocks of the intrusion and residual products of chamber differentiation (Proskuryakov, 1967; Odinets, 1971; Kozlov, 1973), independent sills (Osokin, personal communication), or deeply reworked xenoliths of metavolcanic rocks of the Kuksha Formation of the Imandra–Varzuga zone (Borisova *et al.*, 1999).

In this paper, we present new petrographic and geochemical data and attempt to show that the magnetite gabbro is probably a final product in the Fenner differentiation trend of the initial melt of the Western Pansky Tundra layered intrusion. Major attention is focussed on various physicochemical aspects of magnetite gabbro formation.

## REGIONAL POSITION AND STRUCTURE OF THE WESTERN PANSKY TUNDRA INTRUSION

The Western Pansky Tundra intrusion is one of 40 known layered intrusions in northern Karelia (Kola Peninsula) and northern Finland clustering into northern (Kola) and southern (Fenno–Karelian) belts (Alapieti *et al.*, 1990). The intrusion is renowned owing to the occurrence of several sulfide-bearing horizons (reefs) enriched in platinum-group elements (PGE), which are similar in many respects to the famous Merensky and J–M reefs of the Bushveld and Stillwater complexes.

[1] Present address: Institute of Geosciences, University of Oulu, Linnanmaa, FIN-90570, Oulu, Finland; e-mail: Rais.Latypov@oulu.fi.

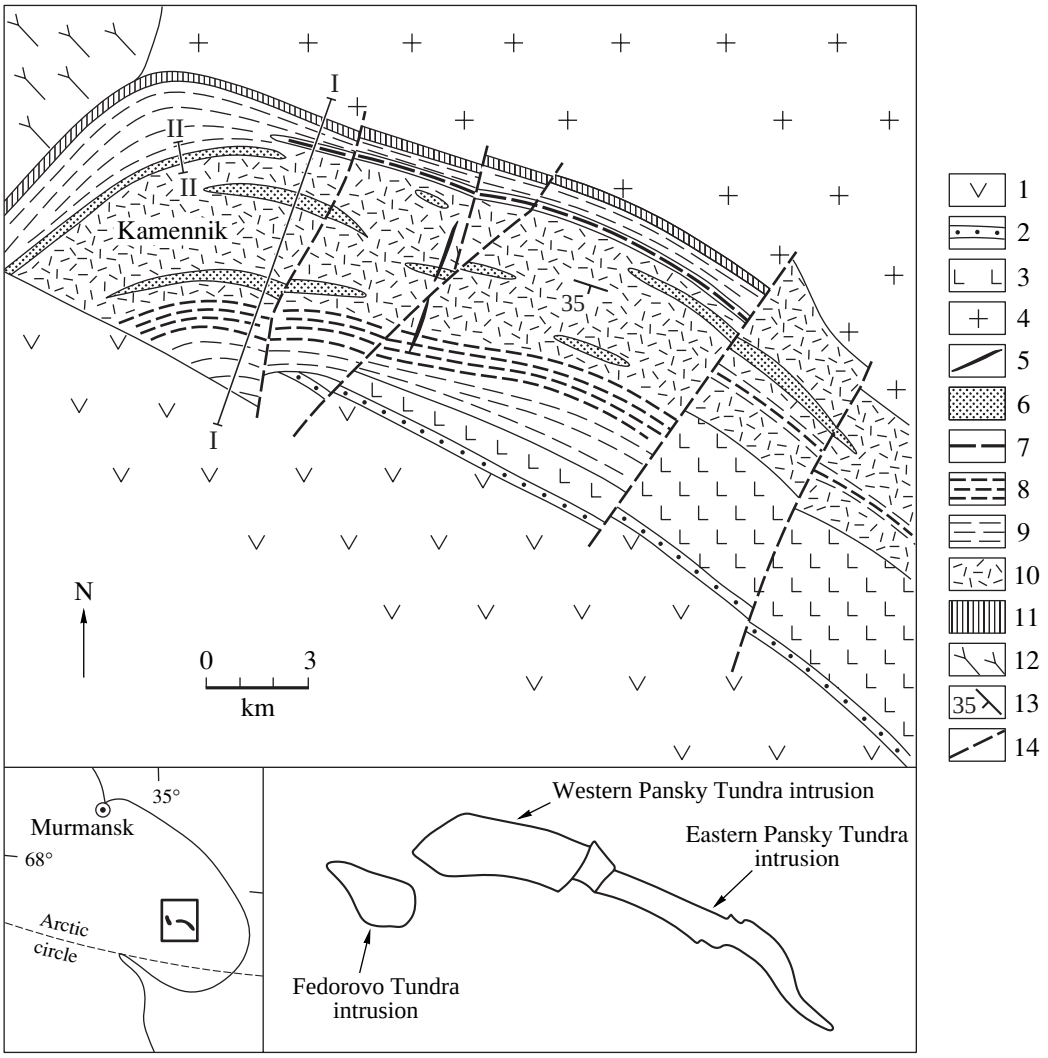


**Fig. 1.** Schematic geologic structure of the Early Proterozoic Western Pansky Tundra intrusion, simplified after Odinets (1971).
1–3, Early Proterozoic volcanic–sedimentary rocks of the Strelna Group of the Imandra–Varzuga zone: 1, meta-andesite of the Seidorechka Formation; 2, quartzite of the Seidorechka Formation; 3, metabasalt of the Kuksha Formation; 4, alkaline granites of the White Tundra; 5, gabbro-dolerite and quartz dolerite dikes; 6–11, intrusion: 6, magnetite gabbro; 7, lower and 8, upper layered horizons; 9, trachytoid and 10, massive rocks of the gabbronorite zone; 11, rocks of the norite zone; 12, Archean gneisses and granitoids of the Keiv block; 13, layering (35°, dip angle); and 14, fault. I–I is the position of the stratigraphic cross-section (Fig. 2) and II–II is the position of the cross-section through the magnetite gabbro of the lower level, northwestern Kamennik area.

This called close attention of researchers to the petrologic aspects of intrusion formation (Mitrofanov *et al.*, 1994; Dokuchaeva, 1994; Korchagin *et al.*, 1994; Abzalov *et al.*, 1993; Balabonin *et al.*, 1994; Latypov, 1994, 1995; Latypov *et al.*, 1999).

According to a currently accepted concept (Dokuchaeva, 1994), the intrusion is part of the Fedorovo–Pansky Massif, which was disjoined into a number of large blocks at the modern erosion level by tectonic dislocations (Fig. 1). The largest are (from west to east) the Fedorovo, Western Pansky Tundra, and Eastern Pansky Tundra blocks. Significant differences were recently found in the character of phase, modal, and cryptic layering in these plutons. This provides a basis for the revision of this concept, and, in this paper, the block of the Western Pansky Tundra is considered as an independent intrusion.

The intrusion of the Western Pansky Tundra extends in a northwestern direction for more than 25 km, is about 80 km$^2$ in area, and dips south-southwest at an angle of 30°–35°. The true thickness of the intrusion is 3–4 km. The age of gabbronorite from the intrusion was determined by the U–Pb method for zircons as 2491 ± 1.5 Ma (Bayanova *et al.*, 1994) and 2501.5 ± 1.4 Ma (Amelin *et al.*, 1995), the anorthosite was dated at 2449 ± 12 Ma (Bayanova *et al.*, 1995); $\varepsilon_{Nd}$ (2487 ± 51 Ma) for the intrusion is 2.1 ± 0.5 (Balashov *et al.*, 1993).

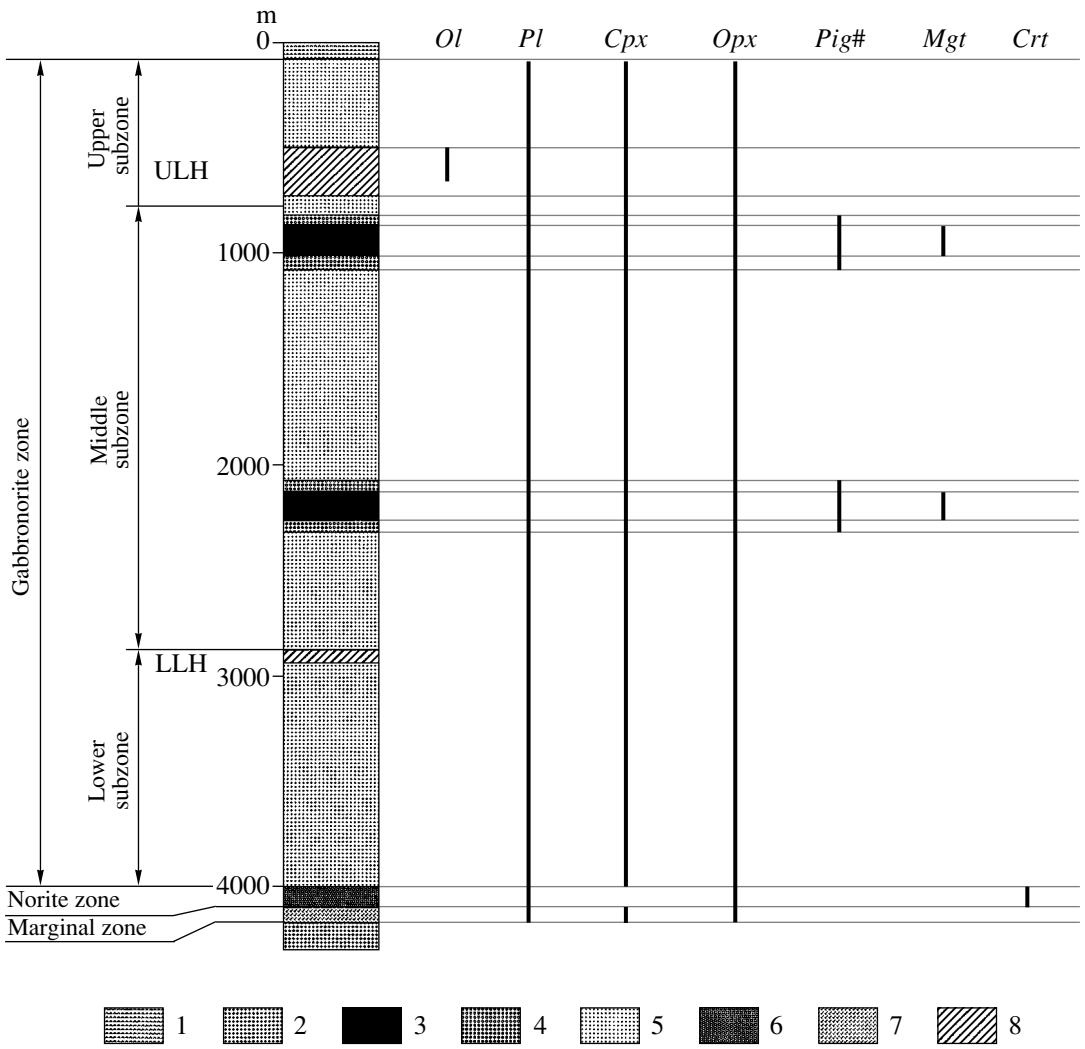


**Fig. 2.** Stratigraphic column for the Western Pansky Tundra intrusion (I–I in Fig. 1) showing intervals of the development of cumulus phases.

1, Volcanic–sedimentary rocks of the Imandra–Varzuga zone; 2, Archean gneisses and granitoids of the Keiv block; 3–8, intrusion rocks: 3, magnetite gabbro with inverted pigeonite (*Pl–Cpx–Opx–Pig#–Mgt* cumulate); 4, gabbronorite with inverted pigeonite (*Pl–Cpx–Opx–Pig#* cumulate); 5, gabbronorite (*Pl–Cpx–Opx* cumulate); 6, norite (*Pl–Opx* cumulate); 7, taxite gabbronorite; and 8, layered horizons. ULH and LLH are the upper and lower layered horizons, respectively.

The structural position of the intrusion is defined by its location in the joining zone of the Archean Keiv block and the Early Proterozoic Imandra–Varzuga zone. The intrusion occur near Archean gneisses only in the ultimate northwestern portion (*Imandra–Varzugskaya zona*, 1982), but no direct contact of the intrusion rocks with the gneisses was found, because of the lack of exposures. The massif is bound by peralkaline granites on the north. The problem of relationships of the Western Pansky Tundra intrusion with the peralkaline granites of the White Tundra (Batieva, 1976; Kozlov, 1973) is probably resolved: according to U–Pb data for zircon, the peralkaline granite of the White Tundra (2606 ± 48 Ma, Bayanova, personal communication) is older than the rocks of the Western Pansky Tundra intrusion.

The joining of the Western Pansky Tundra intrusion with the volcanic and sedimentary rocks of the Imandra–Varzuga zone is covered by Quaternary deposits. The contacts were revealed by drilling and open pits in the southern roof portion of the intrusion. They are secondary tectonic: both intrusive rocks and sedimentary–volcanic sequences are strongly sheared in the contact zone.

The general structure of the Western Pansky Tundra intrusion is relatively simple (Figs. 1, 2). It is dominated by gabbronorite showing variable proportions of rock-forming minerals, textural and structural features. The following zones were recognized in the section from bottom to top:

1. Marginal zone (50–60 m) of taxite gabbronorite (*Pl–Cpx–Opx* cumulate).[2] It contains abundant coarse-grained mafic segregations and xenoliths of the country gneisses assimilated to a varying degree.

2. Norite zone (40–50 m) is dominated by norite (*Pl–Opx* cumulate) with minor plagiopyroxenite (*Opx* cumulate with intercumulus *Pl*). The latter contains chromite mineralization formed by small accessory grains of alumochromite–subferrialumochromite (Dokuchaeva, 1994).

3. Gabbronorite zone (about 4000 m) is dominated by gabbronorite (*Pl–Cpx–Opx* cumulate) with varying grain size, structure, and proportions of cumulus minerals. Three units were distinguished in this zone: lower, middle, and upper subzones.

The lower subzone (1000–1100 m) shows a gradual transition to the underlying norite zone. It is composed of mesocratic trachytoid gabbronorite (*Pl–Cpx–Opx* cumulate), whose trachytoid structure is controlled by the near-parallel orientation of plagioclase laths in a plane. The subzone is terminated by the first horizon of thin-layered rocks, which is referred to as the lower layered horizon (LLH). It is 50–100 m thick and distinguished in the homogeneous gabbronorite section by the contrast intercalation of leucocratic and melanocratic rocks including anorthosite (*Pl* cumulate), leucogabbro (*Pl* cumulate with intercumulus *Cpx* and *Opx*), gabbronorite (*Pl–Opx* cumulate with intercumulus *Cpx*), norite (*Pl–Opx* cumulate), and pyroxenite (*Opx* cumulate with intercumulus *Pl* and *Cpx*) rocks. Low-sulfide PGE mineralization is closely related to the leucogabbro and anorthosite (sometimes olivine-bearing).

The middle subzone (2000–2150 m) is composed mainly of massive gabbronorite (*Pl–Cpx–Opx* cumulate) with gabbro and gabbro ophitic textures. In this subzone, magnetite bodies with inverted pigeonite form layers and lenticular bodies from 20 to 100 m thick and from hundreds of meters to 10 km long. They are grouped into three discontinuous belts, lower, upper, and middle, extended in agreement with the general structural plan of the massif.

The upper subzone (650–700 m) is composed of trachytoid gabbronorite (*Pl–Cpx–Opx* cumulate). The second horizon of thin-layered rocks is located near the basement of this subzone. It is referred to as the Upper Layered Horizon (ULH). The most common rocks in the ULH are gabbronorite (*Pl–Cpx–Opx* cumulate), anorthosite (*Pl* cumulate and *Pl* cumulate with intercumulus *Cpx* and *Opx*), olivine gabbronorite (*Pl–Cpx–Opx–Ol* cumulate), olivine norite (*Pl–Ol–Opx* cumulate), olivine leucogabbronorite (*Pl* cumulate with intercumulus *Ol*, *Cpx*, and *Opx*), and troctolite (*Pl–Ol* cumulate). Several layers of low-sulfide platinum group mineralization were found in the ULH section. The most important of them is related to a thick anorthosite layer of the first sequence.

[2] Abbreviations used in the text and diagrams: *Pl*, plagioclase; *Ol*, olivine; *Opx*, orthopyroxene; *Pig*, pigeonite; *Pig#*, inverted pigeonite; *Cpx*, clinopyroxene; *Qtz*, quartz; *Mgt*, magnetite; *Crt*, chromite; *Amf*, amphibole; *Ap*, apatite; *Ilm*, ilmenite; $P_{H_2O}$, fluid pressure; *f*# = Fe/(Fe + Mg) for mafic minerals; *An* = 100 × *An*/(*An* + *Ab*), anorthite mole fraction of plagioclase; *L*, melt; *Fo*, forsterite; *Fa*, fayalite; *Di*, diopside; *Hd*, hedenbergite; *Ab*, albite; *An*, anorthite; *Or*, orthoclase; $Ol_{25-50}$, olivine with interval of fayalite mole fraction; and $Pl_{60-70}$, plagioclase with interval of anorthite mole fraction.

## METHODS

Three sections were chosen for detailed sampling in the lower, middle, and upper levels of magnetite gabbro at Kamennik Mountain (Fig. 1). We collected 110 samples for chemical analysis from bedrock exposures. The samples were from 1 to 2 kg, at an average of about 1.5 kg. All the rocks are fresh and almost unaltered. Major and trace elements were analyzed by the atom absorption and spectral methods in the Geological Institute, Kola Research Center, Russian Academy of Sciences, Russia. The minerals were analyzed on the Cameca electron microprobe of the same institute. The silicate analyses were recalculated to CIPW norms and a number of additional petrochemical parameters. The following petrochemical parameters were used for the deciphering of the differentiation characteristics: Sum(*Fsp*), sum of normative feldspars; *F*#, total Fe/(Fe + Mg) ratio; *f*(hy), Fe/(Fe + Mg) ratio of normative orthopyroxene; *F*(ox), degree of iron oxidation; *An*(norm), anorthite mole fraction of normative plagioclase; and K(hy), normative pyroxene ratio. Because of the similar character of cryptic layering in all the sections, we consider only one body from the lower level. The analyses of rocks and minerals from this body (Tables 1–4) were used for the construction of stratigraphic columns (Figs. 3, 4).

## IGNEOUS STRATIGRAPHY AND PETROGRAPHY OF MAGNETITE GABBRO

The data of previous researchers (Proskuryakov, 1967; Odinets, 1971; Kozlov, 1973) and our observations suggest that the transition from the magnetite gabbro to the enclosing gabbronorite is mostly gradual. Only in one instance, we observed a relatively sharp transition within an interval of about 5–8 m. In general, the transition from the enclosing rocks to magnetite gabbro bodies is characterized by the following sequence:

Zone 1. Gabbronorite with gabbro or gabbro-ophitic textures. These rocks are predominant in the central part of the intrusion and are *Pl–Cpx–Opx* cumulates composed of *Pl*, 47–56%; *Cpx*, 21–32%; and *Opx*, 18–22%.

Zone 2. Gabbronorite with the poikilitic texture. The layers are from 5 to 15 m thick. The zone is not very common; in particular, it is missing near the magnetite gabbro bodies of the lower level. A distinctive feature of the poikilitic gabbronorite is the presence of

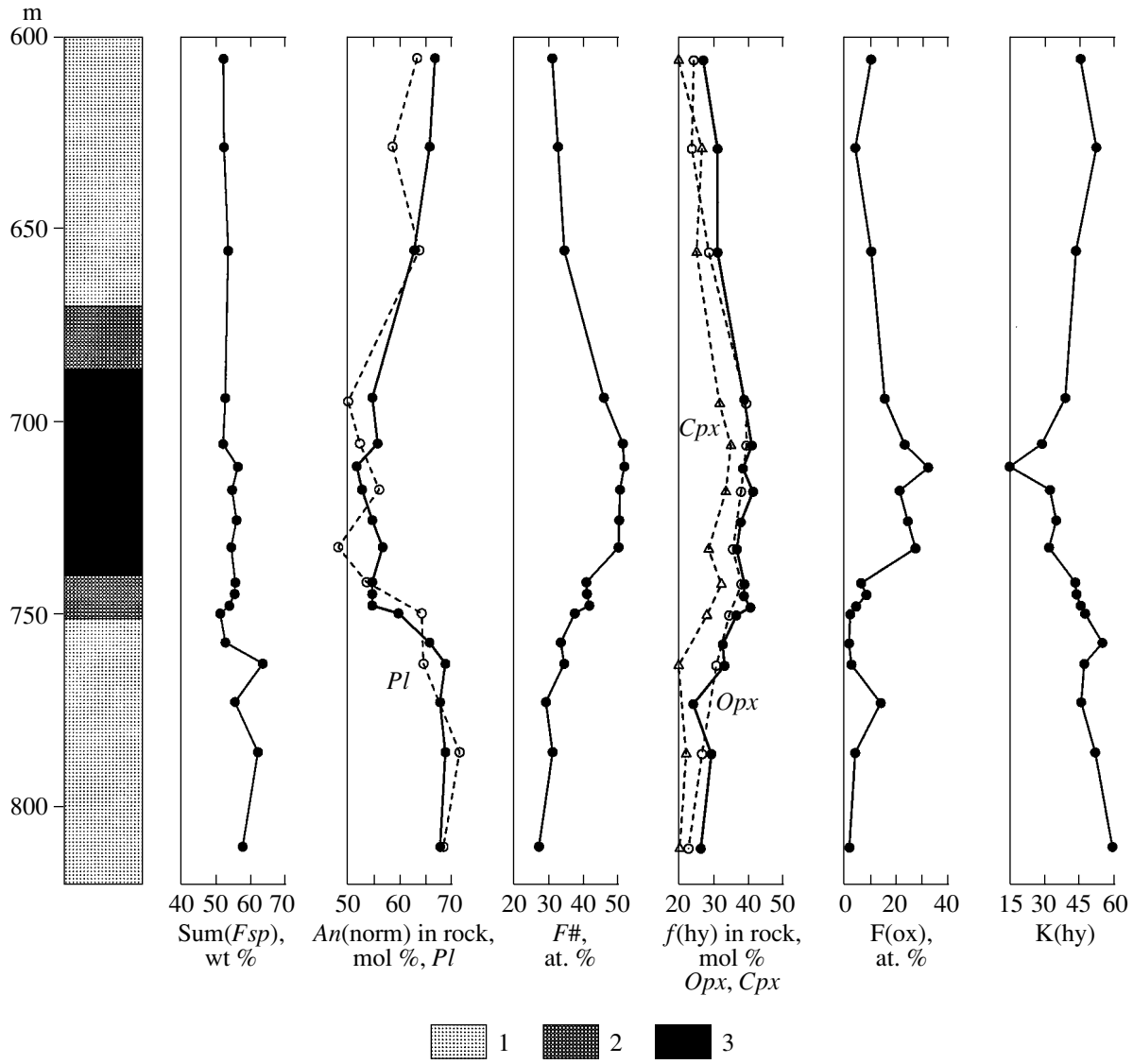


**Fig. 3.** Variations of rock and mineral compositions in the vertical section of the magnetite gabbro of the lower level, northwestern Kamennik area (II–II, Fig. 1).

The depths differ from those in Fig. 2 because of different reference levels. 1, Gabbronorite (*Pl–Cpx–Opx* cumulate); 2, gabbronorite with inverted pigeonite (*Pl–Cpx–Opx–Pig#* cumulate); and 3, magnetite gabbro with inverted pigeonite (*Pl–Cpx–Opx–Pig#–Mgt* cumulate). Sum(*Fsp*) = *Ab* + *Or* + *An*; *An*(norm) = 100 × *An*/(*An* + *Ab*); *F*# = 100 × ($Fe^{2+}$ + $Fe^{3+}$)/($Fe^{2+}$ + $Fe^{3+}$ + Mg); *f*(*hy*) = 100 × *Fs*/(Fs + *En*); *F*(ox) = 100 × $Fe^{3+}$/($Fe^{2+}$ + $Fe^{3+}$); K(hy) = 100 × *Opx*/(*Opx* + *Cpx*).

rounded orthopyroxene grains, 0.5–1.0 cm in size, which show irregular patchy distribution. The orthopyroxene contains inclusions of plagioclase, which are concentrated mainly in the outer parts of orthopyroxene grains. Such a morphology of orthopyroxene is probably due to intense overgrowing of initial cumulus crystals from intercumulus liquid. On this ground, this gabbronorite variety was considered as a three-mineral cumulate. The mineral composition of the rock is the following: *Pl*, 50–59%; *Cpx*, 25–30%; and *Opx*, 12–17%. Magnetite occurs as individual grains rarely accounting for up to 0.5–1.0%.

Zone 3. Gabbronorite with inverted pigeonite. In addition to orthopyroxene, a new liquidus phase appears, pigeonite, whose exsolution produces orthopyroxene with clinopyroxene lamellae at subsolidus temperatures. The rock is a *Pl–Cpx–Opx–Pig#* cumulate containing 50–59% *Pl*, 30–34% *Cpx*, 3–5% *Opx*, and 5–10% *Pig#*. The concentration of magnetite is higher than in the previous zone attaining 1–2%.

Zone 4. Magnetite gabbro with inverted pigeonite. Magnetite first appears in this rock as a liquidus phase. Megascopically, the magnetite gabbro is a dark gray, almost black rock with massive or occasionally trachytoid structures. They differ clearly from the majority of

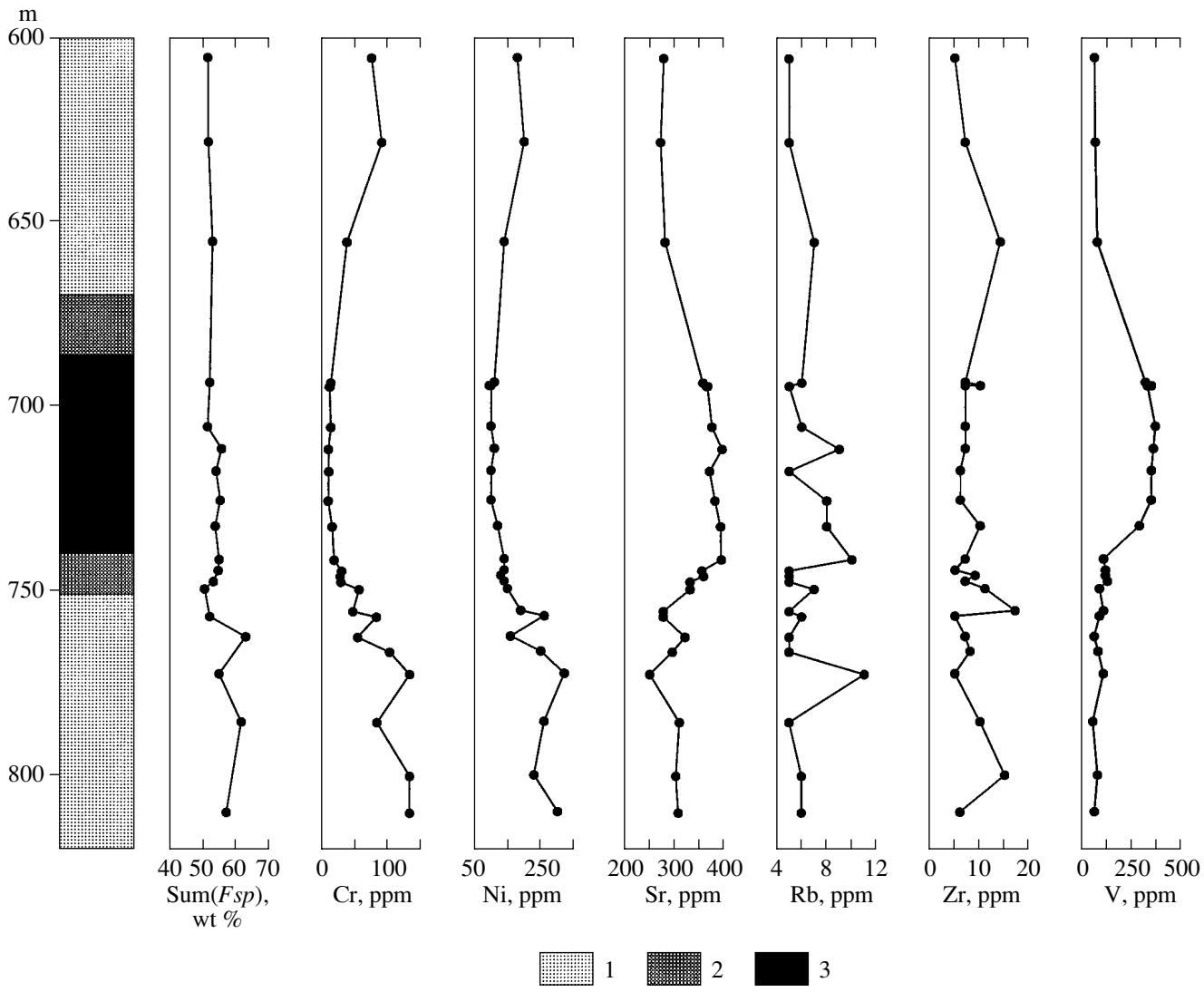


**Fig. 4.** Variations of minor element contents in the vertical section of the magnetite gabbro of the lower level, northwestern Kamennik area (II–II, Fig. 1). Symbols are the same as in Fig. 3.

rocks composing the intrusion by their fine-grained texture. However, the intrusion also contains individual bodies of magnetite gabbro with medium-grained or even pegmatoid textures. The rock is a *Pl–Cpx–Opx–Pig#–Mgt* cumulate containing 54–55% *Pl*, 29–34% *Cpx*, 1–3% *Opx*, 2–5% *Pig#*, and 3–12% *Mgt*.

According to Odinets (1971), the composition of the magnetite gabbro changes regularly from margins to the center of the bodies; the amount of clinopyroxene increases on the expense of orthopyroxene (pigeonite); the concentrations of ilmenite and magnetite increase from 1–2% to 10–12%; while the grain size of rock-forming minerals decreases from 0.5–3.0 to 0.01–0.1 mm. Opaque minerals are represented by ilmenite and magnetite; the latter is significantly predominant over ilmenite accounting for 75 to 90% of opaque minerals. Magnetite occasionally forms veinlike segregations, up to 10–15 cm thick and up to 1–2 m long.

In contrast to the middle and lower levels, the magnetite gabbro of the upper level contains olivine. The olivine-bearing magnetite gabbro is readily distinguished from olivine-free varieties by the presence of characteristic olivine “humps” on the weathered surface and thin veins and stringers of *Pl–Pig#–Cpx–Ol–Mgt* composition, which are abundant in some local areas. In the magnetite gabbro, olivine forms large segregations, up to 1 cm and more, which contain numerous grains of cumulus plagioclase, clinopyroxene, and pigeonite. The distribution of olivine in the rock is very irregular and its content varies from 0 to 5–8%. The poikilitic habit of olivine grains and its occurrence in the veinlike bodies suggest that olivine crystallized from residual intercumulus liquid in the magnetite gabbro bodies.

**Table 1.** Chemical compositions (wt %) and CIPW norms of rocks from the northwestern Kamennik area, lower magnetite gabbro belt

| Component | ka-139/1* | ka-139/2 | ka-139/3 | ka-139/4 | ka-139/6 | ka-139/7 | ka-139/8 | ka-139/9 | ka-139/10 |
|---|---|---|---|---|---|---|---|---|---|
| | 608** | 631 | 658 | 696 | 708 | 714 | 720 | 728 | 735 |
| $SiO_2$ | 52.30 | 51.58 | 51.21 | 50.92 | 48.54 | 47.13 | 49.42 | 49.80 | 48.76 |
| $TiO_2$ | 0.18 | 0.18 | 0.24 | 0.47 | 0.84 | 1.02 | 0.77 | 0.73 | 0.78 |
| $Al_2O_3$ | 15.48 | 15.55 | 15.55 | 14.30 | 13.83 | 14.27 | 14.37 | 14.83 | 14.38 |
| $Fe_2O_3$ | 0.77 | 0.32 | 0.87 | 1.79 | 3.19 | 4.36 | 2.81 | 3.19 | 3.68 |
| FeO | 6.23 | 7.44 | 7.31 | 8.98 | 10.23 | 9.83 | 9.97 | 8.97 | 9.18 |
| MnO | 0.12 | 0.13 | 0.13 | 0.17 | 0.20 | 0.19 | 0.19 | 0.16 | 0.19 |
| MgO | 8.81 | 8.94 | 8.42 | 6.94 | 6.58 | 6.34 | 6.44 | 6.41 | 6.71 |
| CaO | 12.94 | 12.34 | 12.81 | 12.33 | 12.61 | 12.40 | 11.90 | 12.19 | 12.42 |
| $Na_2O$ | 1.84 | 1.90 | 2.09 | 2.49 | 2.32 | 2.68 | 2.65 | 2.62 | 2.41 |
| $K_2O$ | 0.14 | 0.11 | 0.16 | 0.13 | 0.10 | 0.13 | 0.11 | 0.11 | 0.11 |
| $H_2O^-$ | 0.19 | 0.21 | 0.16 | 0.15 | 0.15 | 0.13 | 0.11 | 0.09 | 0.13 |
| LOI | 0.85 | 0.97 | 0.85 | 0.87 | 0.99 | 1.11 | 1.00 | 0.91 | 0.89 |
| $P_2O_5$ | <0.01 | 0.01 | 0.03 | 0.02 | 0.01 | 0.01 | 0.01 | 0.02 | 0.03 |
| Total | 99.86 | 99.68 | 99.83 | 99.56 | 99.59 | 99.60 | 99.75 | 100.03 | 99.67 |
| *Ap* | | 0.02 | 0.07 | 0.05 | 0.02 | 0.02 | 0.02 | 0.05 | 0.07 |
| *Ilm* | 0.34 | 0.34 | 0.46 | 0.89 | 1.60 | 1.94 | 1.46 | 1.39 | 1.48 |
| *Mgt* | 1.12 | 0.46 | 1.26 | 2.60 | 4.63 | 6.32 | 4.08 | 4.63 | 5.34 |
| *Or* | 0.83 | 0.65 | 0.95 | 0.77 | 0.59 | 0.77 | 0.65 | 0.65 | 0.65 |
| *Ab* | 15.56 | 16.07 | 17.68 | 21.06 | 19.62 | 22.67 | 22.41 | 22.16 | 20.38 |
| *An* | 33.57 | 33.58 | 32.58 | 27.46 | 27.03 | 26.53 | 26.99 | 28.38 | 28.10 |
| *En* | 13.88 | 15.42 | 12.14 | 9.65 | 6.22 | 1.19 | 6.54 | 7.91 | 7.32 |
| *Fs* | 6.79 | 9.25 | 7.27 | 8.13 | 5.75 | 0.99 | 6.15 | 6.41 | 5.65 |
| *Di* | 17.36 | 14.73 | 16.45 | 15.92 | 16.20 | 16.65 | 14.51 | 15.38 | 16.34 |
| *Hd* | 7.41 | 7.70 | 8.59 | 11.69 | 13.05 | 12.06 | 11.88 | 10.86 | 10.98 |
| *Qtz* | 1.95 | 0.27 | | | | | | | |
| *Fo* | | | 0.83 | 0.17 | 1.85 | 4.82 | 1.94 | 0.64 | 1.26 |
| *Fa* | | | 0.55 | 0.16 | 1.89 | 4.41 | 2.00 | 0.57 | 1.07 |
| F(ox) | 10.01 | 3.73 | 9.91 | 15.29 | 23.08 | 32.16 | 21.44 | 24.66 | 27.34 |
| *F#* | 30.60 | 32.67 | 34.49 | 46.00 | 51.47 | 51.92 | 50.68 | 50.47 | 50.33 |
| Sum(*Fsp*) | 51.32 | 51.50 | 52.76 | 51.88 | 51.23 | 55.46 | 53.78 | 55.06 | 53.54 |
| *f*(hy) | 27.13 | 31.33 | 31.30 | 39.06 | 41.28 | 38.74 | 41.70 | 38.14 | 36.98 |
| *An*(norm) | 67 | 66 | 63 | 55 | 56 | 52 | 53 | 55 | 57 |
| K(hy) | 45.49 | 52.38 | 43.67 | 39.16 | 29.04 | 7.08 | 32.48 | 35.31 | 32.20 |
| Ni | 180 | 200 | 140 | 110 | 100 | 110 | 100 | 100 | 120 |
| Cr | 73 | 88 | 36 | 12 | 12 | 8.2 | 8.9 | 7.9 | 14 |
| V | 75 | 78 | 88 | 330 | 380 | 370 | 360 | 360 | 300 |
| Zr | 5 | 7 | 14 | 7 | 7 | 7 | 6 | 6 | 10 |
| Sr | 279 | 272 | 281 | 357 | 375 | 395 | 370 | 381 | 392 |
| Rb | 5 | 5 | 7 | 6 | 6 | 9 | 5 | 8 | 8 |

**Table 1.** (Contd.)

| Component | ka-139/11 | ka-139/12 | ka-139/14 | ka-139/15 | ka-139/17 | ka-139/18 | ka-139/20 | ka-139/21 | ka-139/23 |
|---|---|---|---|---|---|---|---|---|---|
| | 744 | 747 | 750 | 752 | 759.5 | 765 | 775 | 788 | 812.5 |
| $SiO_2$ | 52.06 | 51.76 | 52.12 | 52.13 | 51.99 | 51.75 | 50.77 | 52.02 | 51.89 |
| $TiO_2$ | 0.16 | 0.16 | 0.17 | 0.20 | 0.16 | 0.15 | 0.16 | 0.16 | 0.12 |
| $Al_2O_3$ | 15.46 | 15.33 | 14.94 | 14.69 | 15.56 | 19.20 | 16.29 | 18.81 | 17.38 |
| $Fe_2O_3$ | 0.62 | 0.85 | 0.46 | 0.21 | 0.14 | 0.17 | 1.01 | 0.26 | 0.13 |
| FeO | 8.32 | 8.60 | 9.05 | 8.39 | 7.48 | 5.57 | 5.58 | 5.40 | 5.84 |
| MnO | 0.17 | 0.17 | 0.19 | 0.18 | 0.11 | 0.10 | 0.07 | 0.10 | 0.11 |
| MgO | 7.01 | 7.22 | 7.19 | 7.98 | 8.47 | 6.10 | 8.82 | 7.01 | 8.98 |
| CaO | 11.93 | 11.70 | 11.62 | 12.18 | 11.72 | 13.00 | 12.96 | 12.60 | 11.83 |
| $Na_2O$ | 2.70 | 2.68 | 2.64 | 2.18 | 2.56 | 2.23 | 1.23 | 2.04 | 1.99 |
| $K_2O$ | 0.12 | 0.13 | 0.15 | 0.13 | 0.16 | 0.13 | 0.20 | 0.14 | 0.14 |
| $H_2O^-$ | 0.18 | 0.12 | 0.16 | 0.20 | 0.22 | 0.21 | 0.31 | 0.18 | 0.23 |
| LOI | 0.79 | 0.84 | 0.87 | 1.16 | 1.32 | 1.08 | 2.37 | 1.02 | 1.20 |
| $P_2O_5$ | 0.02 | 0.02 | 0.01 | 0.02 | 0.01 | 0.01 | 0.01 | 0.01 | 0.01 |
| Total | 99.54 | 99.58 | 99.57 | 99.65 | 99.90 | 99.70 | 99.78 | 99.75 | 99.85 |
| *Ap* | 0.05 | 0.05 | 0.02 | 0.05 | 0.02 | 0.02 | 0.02 | 0.02 | 0.02 |
| *Ilm* | 0.30 | 0.30 | 0.32 | 0.38 | 0.30 | 0.29 | 0.30 | 0.30 | 0.23 |
| *Mgt* | 0.90 | 1.23 | 0.67 | 0.30 | 0.20 | 0.25 | 1.47 | 0.38 | 0.19 |
| *Or* | 0.71 | 0.77 | 0.89 | 0.77 | 0.95 | 0.77 | 1.18 | 0.83 | 0.83 |
| *Ab* | 22.83 | 22.67 | 22.33 | 18.44 | 15.98 | 18.27 | 15.90 | 17.84 | 16.83 |
| *An* | 29.71 | 29.42 | 28.48 | 29.92 | 33.50 | 42.31 | 35.42 | 41.44 | 38.08 |
| *En* | 10.11 | 10.04 | 10.68 | 12.94 | 15.13 | 9.88 | 14.09 | 12.11 | 16.91 |
| *Fs* | 8.59 | 8.46 | 9.73 | 9.93 | 9.73 | 6.52 | 5.96 | 6.68 | 8.04 |
| *Di* | 13.87 | 13.51 | 13.37 | 14.93 | 12.84 | 11.45 | 16.96 | 11.51 | 11.74 |
| *Hd* | 10.26 | 9.92 | 10.62 | 9.98 | 7.20 | 6.59 | 6.25 | 5.53 | 4.86 |
| *Qtz* | | | | 0.66 | 1.83 | 2.00 | 0.20 | 1.97 | 0.70 |
| *Fo* | 0.64 | 1.17 | 0.71 | | | | | | |
| *Fa* | 0.59 | 1.09 | 0.72 | | | | | | |
| F(ox) | 6.44 | 8.52 | 4.49 | 2.20 | 1.66 | 2.67 | 14.01 | 4.15 | 1.96 |
| *F#* | 40.97 | 41.11 | 41.83 | 37.63 | 33.51 | 34.49 | 29.22 | 31.09 | 27.13 |
| Sum(*Fsp*) | 54.72 | 54.47 | 53.00 | 50.35 | 51.91 | 62.74 | 54.71 | 61.39 | 56.89 |
| *f*(hy) | 39.25 | 39.06 | 40.95 | 36.85 | 32.86 | 33.44 | 24.33 | 29.56 | 26.55 |
| *An*(norm) | 55 | 55 | 55 | 60 | 66 | 69 | 68 | 69 | 68 |
| K(hy) | 43.66 | 44.12 | 45.97 | 47.88 | 55.38 | 47.61 | 46.35 | 52.45 | 60.05 |
| Ni | 140 | 140 | 140 | 150 | 260 | 160 | 320 | 260 | 300 |
| Cr | 17 | 28 | 27 | 54 | 80 | 52 | 130 | 81 | 130 |
| V | 120 | 130 | 140 | 100 | 100 | 74 | 120 | 67 | 76 |
| Zr | 7 | 5 | 7 | 11 | 5 | 7 | 5 | 10 | 6 |
| Sr | 394 | 355 | 331 | 331 | 278 | 321 | 251 | 310 | 308 |
| Rb | 10 | 5 | 5 | 7 | 6 | 5 | 11 | 5 | 6 |

Note: ka-139/1–ka-139/3 and ka-139/15–ka-139/23, gabbronorites; ka-139/11–ka-139/14, gabbronorites with inverted pigeonite; ka-139/4–ka-139/10, magnetite gabbros with inverted pigeonite. Sum(*Fsp*) = *Ab* + *Or* + *An*; *An*(norm) = 100 × *An*/(*An* + *Ab*); *F#* = 100 × $(Fe^{2+} + Fe^{3+})/(Fe^{2+} + Fe^{3+} + Mg)$; *f*(hy) = 100 × *Fs*/(*Fs* + *En*); K(hy) = 100 × *Opx*/(*Opx* + *Cpx*); F(ox) = 100 × $Fe^{3+}/(Fe^{2+} + Fe^{3+})$.

Here and in Tables 2–4: * Sample no.; **depth, m.

**Table 2.** Composition of plagioclase from the northwestern Kamennik area, wt %

| Component | ka-139/1 | ka-139/2 | ka-139/3 | ka-139/5 | ka-139/6 | ka-139/8 | ka-139/10 | ka-139/11 | ka-139/15 | ka-139/18 | ka-139/21 | ka-139/23 |
|---|---|---|---|---|---|---|---|---|---|---|---|---|
| | 608 | 631 | 658 | 697 | 708 | 720 | 735 | 744 | 752 | 765 | 788 | 812.5 |
| $SiO_2$ | 52.31 | 52.56 | 51.76 | 54.83 | 55.77 | 54.33 | 54.66 | 53.51 | 52.96 | 53.23 | 49.94 | 51.14 |
| $Al_2O_3$ | 29.52 | 29.50 | 29.64 | 27.89 | 27.71 | 27.48 | 28.43 | 29.20 | 29.93 | 30.03 | 31.03 | 30.44 |
| FeO | 0.61 | 0.42 | 0.54 | 0.47 | 0.65 | 0.45 | 0.52 | 0.62 | 0.22 | 0.31 | 0.55 | 0.34 |
| CaO | 12.48 | 12.01 | 13.55 | 10.80 | 10.82 | 11.92 | 10.00 | 10.86 | 12.35 | 12.55 | 14.88 | 14.05 |
| $Na_2O$ | 3.89 | 4.58 | 4.15 | 5.77 | 5.39 | 5.11 | 5.88 | 5.12 | 3.70 | 3.70 | 3.18 | 3.50 |
| $K_2O$ | 0.13 | 0.09 | 0.10 | 0.16 | 0.12 | 0.11 | 0.13 | 0.12 | 0.08 | 0.10 | 0.08 | 0.07 |
| Total | 98.93 | 99.16 | 99.74 | 99.92 | 100.51 | 99.40 | 99.62 | 99.43 | 99.24 | 99.92 | 99.66 | 99.54 |
| Formulas for 8(O) | | | | | | | | | | | | |
| Si | 2.398 | 2.403 | 2.367 | 2.483 | 2.506 | 2.478 | 2.477 | 2.435 | 2.409 | 2.407 | 2.292 | 2.339 |
| Al | 1.595 | 1.589 | 1.597 | 1.489 | 1.468 | 1.478 | 1.519 | 1.566 | 1.605 | 1.601 | 1.679 | 1.641 |
| Fe | 0.024 | 0.016 | 0.021 | 0.018 | 0.024 | 0.017 | 0.020 | 0.023 | 0.008 | 0.012 | 0.021 | 0.013 |
| Ca | 0.613 | 0.588 | 0.664 | 0.524 | 0.521 | 0.583 | 0.486 | 0.529 | 0.602 | 0.608 | 0.732 | 0.689 |
| Na | 0.345 | 0.406 | 0.368 | 0.507 | 0.469 | 0.452 | 0.517 | 0.452 | 0.327 | 0.324 | 0.283 | 0.311 |
| K | 0.007 | 0.005 | 0.006 | 0.010 | 0.007 | 0.007 | 0.007 | 0.007 | 0.005 | 0.006 | 0.005 | 0.004 |
| *Or* | 0.73 | 0.50 | 0.58 | 0.96 | 0.70 | 0.67 | 0.69 | 0.71 | 0.54 | 0.64 | 0.49 | 0.40 |
| *Ab* | 35.75 | 40.64 | 35.45 | 48.70 | 47.04 | 43.38 | 51.19 | 45.75 | 35.01 | 34.54 | 27.75 | 30.98 |
| *An* | 63.52 | 58.86 | 63.97 | 50.34 | 52.26 | 55.95 | 48.12 | 53.54 | 64.45 | 64.82 | 71.76 | 68.63 |

Note: ka-139/1–ka-139/3 and ka-139/15–ka-139/23, gabbronorites; ka-139/11, gabbronorite with inverted pigeonite; ka-139/5–ka-139/10, magnetite gabbro with inverted pigeonite.

## CRYPTIC VARIATIONS OF ROCK AND MINERAL COMPOSITIONS THROUGH THE SECTION OF MAGNETITE GABBRO OF THE LOWER LEVEL

Any chemical discontinuity between the magnetite gabbro and enclosing rocks could have been considered as a decisive argument for the epigenetic nature (xenoliths or sills) of the former. The opposite would evidently serve as evidence for the syngenetic origin of the magnetite gabbro as final differentiation products. Variation diagrams showing the differentiation parameters of rocks and minerals as functions of sample position in the vertical section of the intrusion (Fig. 3) are most convenient for the comparison of chemical compositions. It is evident that toward the center of the body, there is a gradual decrease in the normative and real anorthite content of plagioclase (from *An* = 65–70% to *An* = 48–52%), a regular decrease in the total and partial Fe/(Fe + Mg) ratio of orthopyroxene and clinopyroxene [from *f*(hy) = 22–25% to *f*(hy) = 38–42%], and a decrease in the pyroxene ratio [from *K*(hy) = 50–60% to *K*(hy) = 30–35%, except for a single point with *K*(hy) = 8%]. The body of magnetite gabbro is clearly distinguished in the section by a sharp increase in the degree of iron oxidation, *F*(ox), which results in the appearance of a new cumulus phase, magnetite.

The gradual transition from the enclosing gabbronorite to magnetite gabbro is pointed out by the distribution of a number of minor elements (Fig. 4). Toward the central parts of the bodies, there is a stable trend of gradual decline of Cr (from 125 to 3–15 ppm) and Ni (from 275 to 90–100 ppm) contents and simultaneous increase in Sr (from 275–310 to 370–400 ppm). The later effect is probably related to the well-known trend of plagioclase enrichment in Sr with increasing albite mole fraction (Ashwal, 1993). The deviation of individual points from the general trend in various directions is related to variations of plagioclase amount in the rocks, as suggested by changes in the parameter Sum(*Fsp*). Worth noting is the lack of distinct trends on the diagrams for some incompatible elements, in particular, Zr and Rb. Their concentrations in the magnetite gabbro and enclosing gabbronorite are similar and are generally close to the detection limit of the analytical method (5 ppm). The boundaries of magnetite gabbro bodies are clearly outlined by a sharp increase in the content of V, which is concentrated in magnetite.

The continuous evolution trends of changes in rock composition from the gabbronorite to magnetite gabbro

**Table 3.** Composition of orthopyroxene from the northwestern Kamennik area, wt %

| Component | ka-139/1 | ka-139/2 | ka-139/3 | ka-139/5 | ka-139/6 | ka-139/8 | ka-139/10 | ka-139/11 | ka-139/15 | ka-139/18 | ka-139/21 | ka-139/23 |
|---|---|---|---|---|---|---|---|---|---|---|---|---|
| | 608 | 631 | 658 | 697 | 708 | 720 | 735 | 744 | 752 | 765 | 788 | 812.5 |
| $SiO_2$ | 54.57 | 54.34 | 53.54 | 52.37 | 52.76 | 53.66 | 52.82 | 51.95 | 53.06 | 54.56 | 54.24 | 54.59 |
| $TiO_2$ | 0.09 | 0.11 | 0.31 | 0.13 | 0.21 | 0.19 | 0.20 | 0.17 | 0.23 | 0.26 | 0.26 | 0.16 |
| $Al_2O_3$ | 1.09 | 1.02 | 0.89 | 0.54 | 0.56 | 0.59 | 0.78 | 1.79 | 0.82 | 0.66 | 0.90 | 0.66 |
| FeO | 15.62 | 16.24 | 17.61 | 23.66 | 23.48 | 22.03 | 21.62 | 22.85 | 21.86 | 18.81 | 16.65 | 14.65 |
| MnO | 0.32 | 0.34 | 0.38 | 0.55 | 0.65 | 0.60 | 0.55 | 0.53 | 0.49 | 0.45 | 0.41 | 0.33 |
| MgO | 27.18 | 24.96 | 24.39 | 20.23 | 20.01 | 20.90 | 21.67 | 20.59 | 22.99 | 23.44 | 25.42 | 27.61 |
| CaO | 1.17 | 2.03 | 2.26 | 2.49 | 1.82 | 1.17 | 1.17 | 1.15 | 1.08 | 1.20 | 1.68 | 1.26 |
| $K_2O$ | n.d. | n.d. | n.d. | n.d. | n.d. | n.d. | n.d. | 0.32 | n.d. | n.d. | n.d. | n.d. |
| $Cr_2O_3$ | 0.04 | 0.04 | n.d. | n.d. | n.d. | n.d. | n.d. | n.d. | 0.02 | n.d. | n.d. | 0.04 |
| CoO | 0.03 | n.d. | 0.04 | n.d. | n.d. | n.d. | n.d. | n.d. | 0.05 | n.d. | n.d. | 0.03 |
| NiO | n.d. | 0.07 | 0.07 | n.d. | n.d. | 0.04 | n.d. | 0.05 | 0.07 | 0.04 | 0.05 | 0.04 |
| Total | 100.11 | 99.15 | 99.49 | 99.95 | 99.48 | 99.18 | 98.81 | 99.40 | 100.67 | 99.42 | 99.61 | 99.37 |
| Formulas for 6(O) | | | | | | | | | | | | |
| Si | 1.968 | 1.988 | 1.970 | 1.977 | 1.994 | 2.009 | 1.988 | 1.960 | 1.963 | 2.008 | 1.979 | 1.976 |
| Ti | 0.002 | 0.003 | 0.008 | 0.004 | 0.006 | 0.005 | 0.006 | 0.005 | 0.006 | 0.007 | 0.007 | 0.004 |
| Al | 0.046 | 0.044 | 0.039 | 0.024 | 0.025 | 0.026 | 0.034 | 0.080 | 0.036 | 0.028 | 0.039 | 0.028 |
| Fe | 0.471 | 0.497 | 0.542 | 0.747 | 0.742 | 0.690 | 0.680 | 0.721 | 0.676 | 0.579 | 0.508 | 0.444 |
| Mn | 0.010 | 0.010 | 0.012 | 0.017 | 0.021 | 0.019 | 0.017 | 0.017 | 0.015 | 0.014 | 0.013 | 0.010 |
| Mg | 1.461 | 1.361 | 1.338 | 1.138 | 1.127 | 1.166 | 1.216 | 1.158 | 1.268 | 1.286 | 1.382 | 1.490 |
| Ca | 0.045 | 0.080 | 0.089 | 0.101 | 0.074 | 0.047 | 0.047 | 0.046 | 0.043 | 0.047 | 0.065 | 0.049 |
| K | | | | | | | | 0.015 | | | | |
| Cr | 0.001 | 0.001 | | | | 0.001 | | | | | | 0.001 |
| Co | 0.001 | | 0.001 | | | | | | 0.001 | | | |
| Ni | | 0.002 | 0.002 | | | 0.001 | | 0.002 | 0.002 | 0.001 | 0.001 | 0.001 |
| *Fs* | 23.82 | 25.64 | 27.53 | 37.61 | 38.19 | 36.26 | 35.00 | 37.45 | 34.02 | 30.28 | 25.98 | 22.39 |
| *En* | 73.90 | 70.23 | 67.95 | 57.30 | 58.00 | 61.27 | 62.58 | 60.16 | 63.81 | 67.26 | 70.69 | 75.14 |
| *Wo* | 2.28 | 4.13 | 4.52 | 5.09 | 3.81 | 2.47 | 2.42 | 2.39 | 2.16 | 2.46 | 3.32 | 2.47 |
| *f#* | 24.38 | 26.75 | 28.83 | 39.63 | 39.70 | 38.18 | 35.86 | 38.37 | 34.77 | 31.05 | 26.88 | 22.96 |

Note: ka-139/1–ka-139/3 and ka-139/15–ka-139/23, gabbronorites; ka-139/11, gabbronorite with inverted pigeonite; ka-139/5—ka-139/10, magnetite gabbros with inverted pigeonite. $f\# = 100 \times Fe/(Fe + Mg)$; n.d., not detected.

can be also illustrated on a number of petrochemical grids. On the *An*(norm)–*F*# diagram (Fig. 5), the points of the magnetite gabbro and enclosing gabbronorite straddle a single trend oriented at a low angle to the boundary line dividing field of Fe–Ca and Mg–Na affinities. It is characterized by the correlated changes in both the parameters, which is typical of rocks formed through crystal fractionation. Similarly, the slightly modified E. Osborn diagram $SiO_2$–*F*# (Fig. 5) shows an almost vertical extended trend in the calc-alkaline series field. The diagrams on Figs. 6a and 6b are also instructive in that the points form an almost continuous trend of increasing total iron content ($FeO + Fe_2O_3$) and simultaneously decreasing MgO and $SiO_2$, which is typical of the Fenner differentiation trend of the initial melt of the intrusion.

Thus, our results clearly demonstrate that the magnetite gabbro is an inherent portion of the section of the Western Pansky Tundra intrusion. This is proved by the gradual regular transitions between this rock and the gabbronorite of the massif. The transition is characterized by (1) phase layering manifested in a change of *Pl–Cpx–Opx* cumulates (gabbronorite) by *Pl–Cpx–Opx–Pig#* (gabbronorite with inverted pigeonite) and

**Table 4.** Composition of clinopyroxene from the northwestern Kamennik area, wt %

| Component | ka-139/1 | ka-139/2 | ka-139/3 | ka-139/5 | ka-139/6 | ka-139/8 | ka-139/11 | ka-139/11 | ka-139/15 | ka-139/18 | ka-139/21 | ka-139/23 |
|---|---|---|---|---|---|---|---|---|---|---|---|---|
| | 608 | 631 | 658 | 697 | 708 | 720 | 744 | 744 | 752 | 765 | 788 | 812.5 |
| $SiO_2$ | 52.91 | 52.28 | 51.60 | 51.94 | 51.57 | 51.38 | 50.89 | 50.91 | 51.67 | 52.48 | 51.91 | 51.93 |
| $TiO_2$ | 0.41 | 0.46 | 0.43 | 0.30 | 0.32 | 0.37 | 0.39 | 0.34 | 0.41 | 0.38 | 0.56 | 0.49 |
| $Al_2O_3$ | 1.57 | 1.82 | 1.90 | 1.42 | 1.21 | 1.41 | 1.52 | n.d. | 1.65 | 1.05 | 1.54 | 1.51 |
| FeO | 6.77 | 8.11 | 8.86 | 10.88 | 12.31 | 12.26 | 14.03 | 11.92 | 9.58 | 7.14 | 7.75 | 7.34 |
| MnO | 0.24 | 0.19 | 0.24 | 0.32 | 0.31 | 0.40 | 0.26 | 0.29 | 0.30 | 0.26 | 0.22 | 0.20 |
| MgO | 15.16 | 14.54 | 14.73 | 13.03 | 13.39 | 13.49 | 13.45 | 13.89 | 13.64 | 15.15 | 15.20 | 16.11 |
| CaO | 22.07 | 21.25 | 20.93 | 20.76 | 20.81 | 20.49 | 19.79 | 20.58 | 21.77 | 23.27 | 22.11 | 21.42 |
| $Na_2O$ | 0.21 | 0.20 | 0.27 | 0.69 | 0.23 | 0.30 | 0.04 | 0.32 | 0.21 | 0.14 | 0.34 | 0.24 |
| $K_2O$ | n.d. | n.d. | n.d. | n.d. | n.d. | n.d. | n.d. | n.d. | n.d. | 0.01 | 0.01 | n.d. |
| $Cr_2O_3$ | n.d. | 0.04 | n.d. | n.d. | n.d. | n.d. | n.d. | n.d. | 0.05 | 0.12 | 0.03 | 0.05 |
| NiO | n.d. | n.d. | 0.02 | 0.04 | n.d. | n.d. | n.d. | 0.03 | n.d. | n.d. | 0.04 | 0.04 |
| Total | 99.35 | 98.89 | 98.98 | 99.36 | 100.16 | 100.10 | 100.38 | 99.74 | 99.28 | 100.00 | 99.71 | 99.32 |
| Formulas for 6(O) | | | | | | | | | | | | |
| Si | 1.965 | 1.959 | 1.941 | 1.966 | 1.948 | 1.941 | 1.924 | 1.931 | 1.949 | 1.951 | 1.937 | 1.937 |
| Ti | 0.011 | 0.013 | 0.012 | 0.008 | 0.010 | 0.011 | 0.011 | 0.010 | 0.012 | 0.011 | 0.016 | 0.014 |
| Al | 0.069 | 0.081 | 0.084 | 0.063 | 0.054 | 0.063 | 0.068 | 0.065 | 0.073 | 0.046 | 0.068 | 0.066 |
| Fe | 0.210 | 0.254 | 0.279 | 0.344 | 0.389 | 0.387 | 0.444 | 0.378 | 0.302 | 0.222 | 0.242 | 0.229 |
| Mn | 0.008 | 0.006 | 0.007 | 0.010 | 0.010 | 0.013 | 0.008 | 0.009 | 0.010 | 0.008 | 0.007 | 0.006 |
| Mg | 0.839 | 0.812 | 0.826 | 0.735 | 0.754 | 0.760 | 0.758 | 0.785 | 0.767 | 0.84 | 0.845 | 0.896 |
| Ca | 0.878 | 0.853 | 0.844 | 0.842 | 0.842 | 0.829 | 0.802 | 0.836 | 0.880 | 0.927 | 0.884 | 0.856 |
| Na | 0.017 | 0.014 | 0.020 | 0.050 | 0.017 | 0.022 | 0.029 | 0.023 | 0.015 | 0.01 | 0.025 | 0.017 |
| Cr | | 0.001 | | | | | | | 0.001 | 0.004 | | 0.001 |
| Ni | | | | | | | | 0.001 | | | 0.001 | 0.001 |
| *Fs* | 10.90 | 13.24 | 14.32 | 17.91 | 19.60 | 19.59 | 22.16 | 18.91 | 15.50 | 11.16 | 12.28 | 11.56 |
| *En* | 43.54 | 42.31 | 42.38 | 38.26 | 37.98 | 38.46 | 37.82 | 39.27 | 39.35 | 42.23 | 42.87 | 45.23 |
| *Wo* | 45.56 | 44.45 | 43.30 | 43.83 | 42.42 | 41.95 | 40.02 | 41.82 | 45.15 | 46.61 | 44.85 | 43.21 |
| *f#* | 20.02 | 23.83 | 25.25 | 31.88 | 34.03 | 33.74 | 36.94 | 32.50 | 28.25 | 20.90 | 22.26 | 20.36 |

Note: ka-139/1–ka-139/3 and ka-139/15–ka-139/23, gabbronorites; ka-139/11, gabbronorite with inverted pigeonite; ka-139/5–ka-139/10, magnetite gabbros with inverted pigeonite. $f\# = 100 \times Fe/(Fe + Mg)$; n.d., not detected.

then directly *Pl–Cpx–Opx–Pig#–Mgt* cumulates (magnetite gabbro with inverted pigeonite); (2) modal layering inferred from a decrease in the abundance of orthopyroxene (pigeonite) and a concurrent increase in clinopyroxene content; and (3) cryptic layering expressed in a stable increase in the partial normative Fe/(Fe + Mg) ratio of orthopyroxene and a continuous decrease in the anorthite fraction of normative plagioclase and Cr and Ni contents of the rocks accompanied by an increase in Sr concentration. In the light of the above three contrasting opinions on the nature of magnetite gabbro, the most appropriate hypothesis is that considering this rock as an ultimate differentiation product of the initial melt of the intrusion (Proskuryakov, 1967: Odinets, 1971; Kozlov, 1973). However, there are a number of physicochemical aspects related to this hypothesis of magnetite gabbro formation that deserve more detailed discussion.

## DISCUSSION

### *Preliminary Notes*

**1. Phase equilibrium diagrams.** For the petrologic analysis, we used isopleth and isobaric isopleth sections of the seven-component system *Fo–Fa–Di–Hd–Ab–An–Qtz* (+$H_2O$) (Figs. 7, 8), which were con-

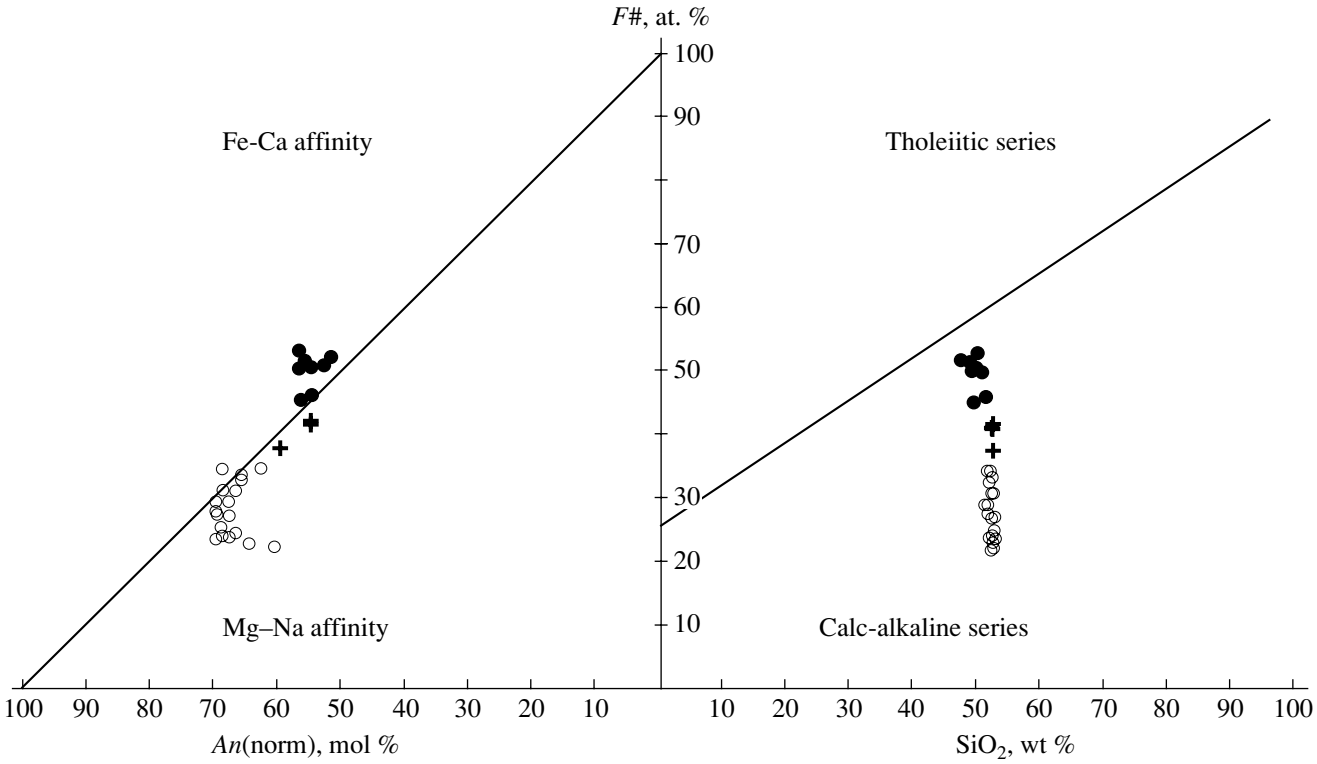


**Fig. 5.** Position of the magnetite gabbro of the lower level and the enclosing rocks on the petrochemical diagram *An*(norm)–*F*#–$SiO_2$ (Dubrovskii, 1998).
Unfilled circles are gabbronorites; crosses, gabbronorites with inverted pigeonite; and filled circles, magnetite gabbros with inverted pigeonite. $An(\text{norm}) = 100 \times An/(An + Ab)$; $F\# = 100 \times (Fe^{2+} + Fe^{3+})/(Fe^{2+} + Fe^{3+} + Mg)$.

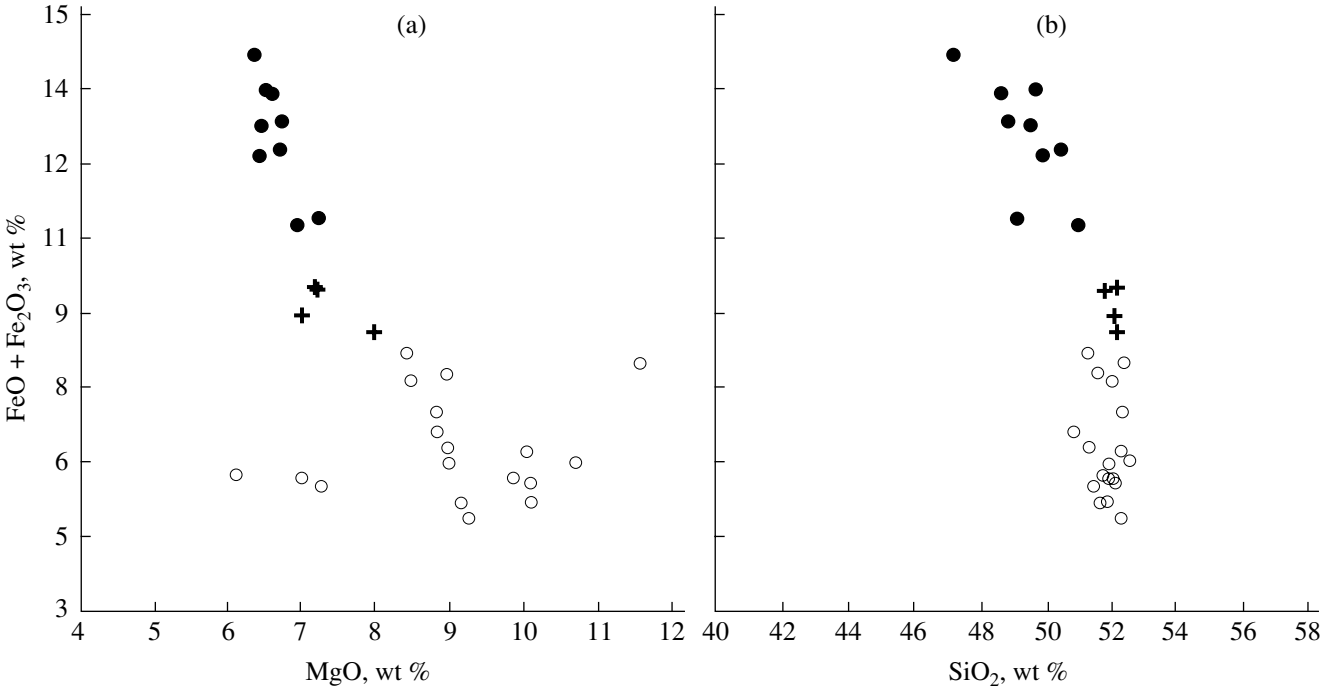


**Fig. 6.** Compositions of the magnetite gabbros and enclosing rocks in the petrochemical diagrams (a) MgO–($FeO + Fe_2O_3$) and (b) $SiO_2$–($FeO + Fe_2O_3$).
Symbols are the same as in Fig. 5.

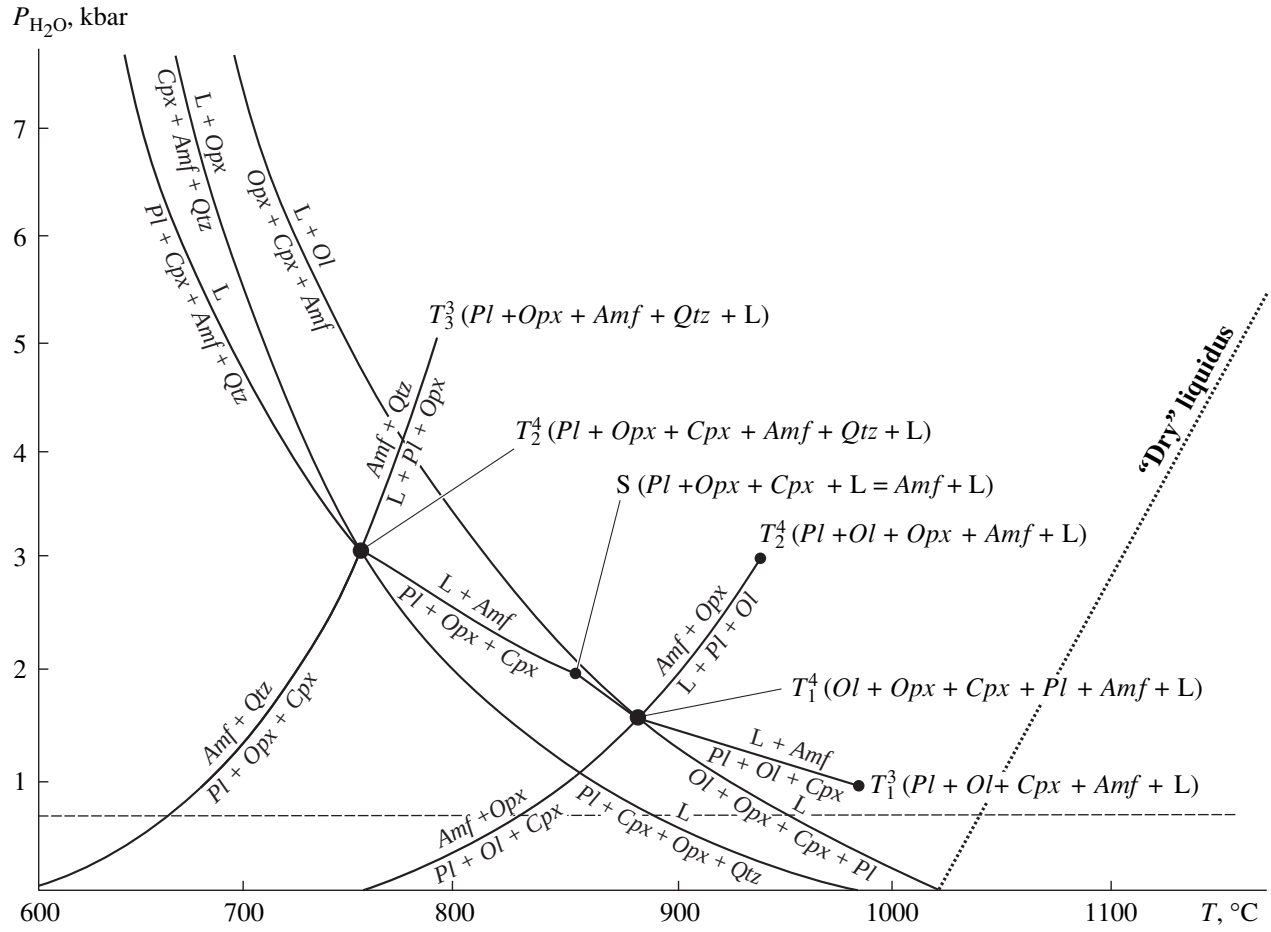


**Fig. 7.** $P_{H_2O}$ –*T* projection of the isopleth section $Ol^{25–50}$–*Cpx*–$Pl^{60–70}$–*Qtz*–$H_2O$ (Dubrovskii, 1993).

The dashed line is the position of the isobaric isopleth section shown in Fig. 8.

structed by the geometric physicochemical techniques (Dubrovskii, 1993, 1998). The procedure is based on the geometrical analysis of physicochemical multisystems, which is described in the fundamental publications of Korzhinskii (1957, 1973) and Zharikov (1976). The choice of the isobaric isopleth section $Ol^{25–50}$–*Cpx*–$Pl^{60–70}$–*Qtz* (+$H_2O$) was based on the observed variations of compositions of cumulus plagioclase and pyroxenes in the intrusion rocks. The diagram is divided by the boundary plane *Opx–Cpx–Pl* (+$H_2O$) into two isopleths: quartz-normative, *Opx–Cpx–Pl–Qtz* (+$H_2O$) and olivine-normative, *Ol–Cpx–Opx–Pl* (+$H_2O$). Each of the isopleths has a respective isobaric invariant point, $E_1^4$ and $E_2^4$. It is substantial that at the values of Fe/(Fe + Mg) of mafic minerals considered and anorthite mole fraction of plagioclase, even at low pressures, the boundary isopleth *Opx–Cpx–Pl* (+$H_2O$) is a thermal divide within a considerable area (orthopyroxene divide) and contains its own gabbronorite eutectic $E_3$, *Opx* + *Cpx* + *Pl* + L. The occurrence of the orthopyroxene thermal divide is related to the cotectic relationships of olivine and orthopyroxene at *f*# of melt from 22 to 78% (Bowen and Schairer, 1935; Longhi and Pan, 1988; Dubrovskii, 1998). Direct application of this isopleth to the solution of petrologic problems is complicated by the difficulty of presentation and interpretation of the diagram. Because of this, we use below simplified projections of this isopleth onto two ternary planes (Fig. 8, right inset) (Dubrovskii, 1998). The position of data points on these projections allow their clear visualization relative to the topologic elements of the diagram in the tetrahedron volume. The techniques of projecting rock composition onto the selected planes was discussed in detail elsewhere (Latypov *et al.*, 1999).

**2. Chamber crystallization of magma under fluid-saturated conditions.** Crucial for the following discussion is the fact that we consider the crystallization of plutonic bodies under the influence of fluid rather than lithostatic pressure. This is related to the known regularities of the mechanism of magma intrusion (Cann, 1970; Fyfe, 1970; Dubrovskii, 1998). The idea is illustrated by Fig. 9, which schematically shows

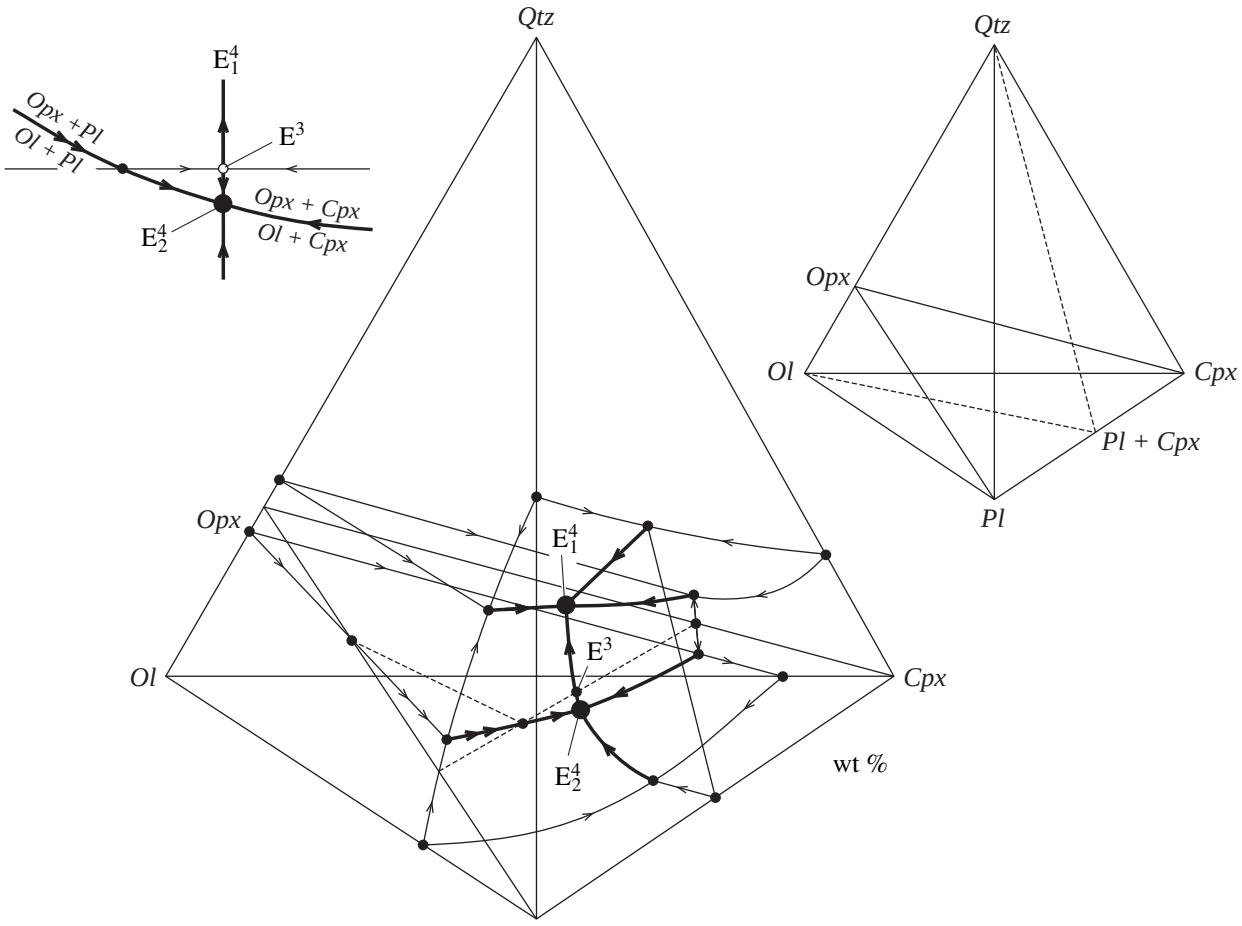


**Fig. 8.** A schematic phase diagram for the isobaric isopleth $Ol^{25–50}$–*Cpx*–$Pl^{60–70}$–*Qtz*–$H_2O$ at $P_{H_2O}$ < 1000 bar (Dubrovskii, 1998).

The upper right inset shows the position of two planes of the diagram used for projecting the points of rock compositions. Cotectic and peritectic lines are denoted by single and double arrows, respectively. Bold liquidus lines are located within the tetrahedron, and thin lines lie on its faces. The upper left inset shows enlarged liquidus relationships in the central part of the phase diagram. $E_1^4$ (*Opx* + *Cpx* + *Pl* + *Qtz* = L); $E_2^4$ (*Ol* + *Opx* + *Cpx* + *Pl* = L); and $E^3$ (*Opx* + *Cpx* + *Pl* = L). The dashed line shows intersection of the surfaces *Ol* + *Opx* + L, *Ol* + *Pl* + L, *Opx* + *Pl* + L, and *Opx* + *Cpx* + L with the plane *Opx*–*Cpx*–*Pl*. See text for explanation.

the position of "dry" and water-saturated liquidus and solidus lines of a silicate system on the *P–T* diagram. "Dry" silicate melts are characterized by liquidus and solidus lines with positive slopes, i.e., their solidus temperature increases with pressure. Hydrous silicate melts show liquidus and solidus lines with negative slopes at low pressure, if the system contains enough water to saturate the liquid. When all the water occurring in the system is dissolved in the melt, the liquidus and solidus lines acquire positive slopes. "Dry" and water-saturated melts behave significantly different during their ascent to the Earth's surface. Dry melt A reaches the surface and erupts as a lava without degassing in point B at significant overheating over its solidus (Fig. 9a). Hydrous melt C, e.g., containing 1 wt % $H_2O$ (Fig. 9b), begins to boil during adiabatic ascent in the moment of intersection of the saturation line at a given water content in the melt in point X, while crystallization starts in point Y (Fyfe, 1970). If the densities of the country rocks and magma are similar in this moment, the magma will be halted and form a plutonic body. Nowadays, it is universally accepted that essentially all natural magmas contain dissolved volatile components dominated by water (Johnson *et al.*, 1994). Thus, Fig. 9 demonstrates that all hydrous magmas responsible for the formation of plutonic bodies give off water during their ascent to the surface forming a separate fluid phase before the onset of crystallization. The water-saturated state of natural magmas is supported by numerous determinations of water contents in melt inclusions from the earliest phenocrysts (e.g., Sobolev, 1997).

The value of water pressure during crystallization of a particular plutonic body is constrained by the presence or absence of cumulus amphibole in the rocks (Hanski, 1992; Dubrovskii, 1998). Let us consider the

*P–T* diagram (Fig. 7). Its characteristic feature is the occurrence of the invariant point $T_1^4$ (*Ol* + *Opx* + *Cpx* + *Pl* + *Amf* + L), where the solidus reaction *Amf* + *Opx* = *Pl* + *Ol* + *Cpx* with a negative slope intersects the liquidus line *Ol* + *Opx* + *Cpx* + *Pl* = L having a positive slope. This point shows the minimum fluid pressure, at which amphibole may occur at the liquidus of the system. According to various authors, this pressure is 1.0–1.5 kbar (Yoder and Tilley, 1962; Condliffe, 1976; Spulber and Rutherford, 1983; Dubrovskii, 1993). Since there is no primary igneous amphibole in the rocks of the Western Pansky Tundra intrusion (Rundkvist, 1999), we can state that the crystallization of rocks occurred at fluid pressures below 1.0–1.5 kbar. At a pressure of about 1 kbar, 1–2 wt % of water (Hamilton *et al.*, 1964; Kadik *et al.*, 1971; Dixon *et al.*, 1995) could be dissolved in the initial melt of the intrusion, which was tholeiitic in composition (Latypov *et al.*, 1999).

### *Physicochemical Aspects of Magnetite Gabbro Formation*

**1. Crystallization trend of intrachamber melt.** The transition from the enclosing gabbronorite to magnetite gabbro is characterized by the following sequence of phase appearance: *Pl* + *Opx* + *Cpx* (gabbronorite) ⟶ *Pl* + *Cpx* + *Opx* + *Pig* (gabbro with inverted pigeonite) ⟶ *Pl* + *Cpx* + *Opx* + *Pig* + *Mgt* (magnetite gabbro with inverted pigeonite). A characteristic feature of this trend is the coexistence of three cumulus pyroxenes in the rock: orthopyroxene, pigeonite, and augite. Such a phenomenon is not common in layered basic–ultrabasic complexes. This is observed when the change from orthopyroxene to pigeonite proceeds during a certain time period of simultaneous crystallization of the two pyroxenes. This is exemplified by the Bushveld complex, where the three-pyroxene assemblage is observed in the rocks of the gabbronorite zone within an almost one-kilometer portion of the section (Gruenewaldt, 1970; Eales and Cawthorn, 1996).

In order to trace the crystallization trend corresponding to the case under consideration, we must extend the phase diagram of the isopleth *Ol–Cpx–Pl–Qtz* (+$H_2O$) introducing the magnetite component (*Mgt*). Unfortunately, we are restricted to the three-dimensional space and cannot visualize the necessary figure with five vertexes. The situation is simplified by the fact that the mineral composition of the gabbronorites and small scatter of data points of the intrusion rocks on the section of the isobaric isopleth (Fig. 10) suggest that the chamber melt was located on the plane of the boundary isopleth *Opx–Cpx–Pl* (+$H_2O$) (Fig. 10a) near the cotectic point $E^3$ (Fig. 10b). The appearance of some points of magnetite gabbro free of normative olivine from the lower level in the olivine-normative isopleth volume is probably an artifact. Most likely, this resulted from underestimation of $Fe_2O_3$ fraction relative to FeO, which provided the appearance of normative olivine end-members at CIPW norm calculation. Therefore, it is sufficient for our purposes to add the component *Mgt* to the isopleth. In such a case, it is possible to show the liquidus relationships between all the phases considered (*Opx*, *Cpx*, *Pig*, *Pl*, and *Mgt*) in the tetrahedron volume *Opx–Cpx–Pl–Mgt* (+$H_2O$). The construction of such a schematic phase diagram is not difficult because *Mgt* behaves as a cotectic phase with all other phases of this isopleth (Dubrovskii, 1998).

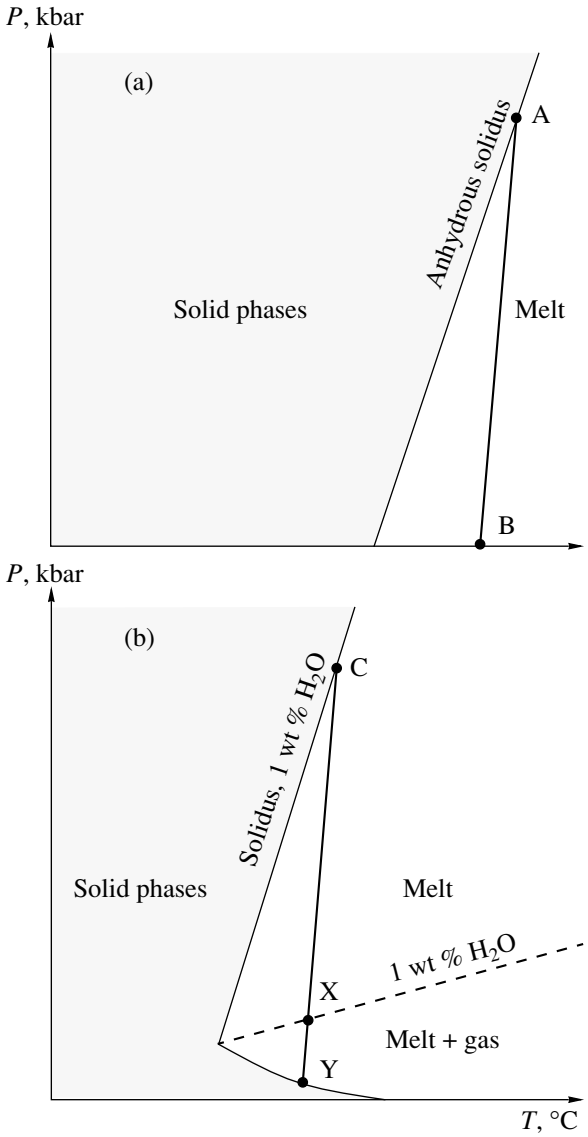


**Fig. 9.** Schematic *P–T* projections of liquidus–solidus equilibria for a "dry" basaltic melt (a) and basaltic melt with 1 wt % $H_2O$ (b), mainly after Fyfe (1972) and Dubrovskii (1993).

The dashed line shows the isopleth with 1 wt % $H_2O$ separating the region with melt from that with melt and fluid phase. See text for explanation.

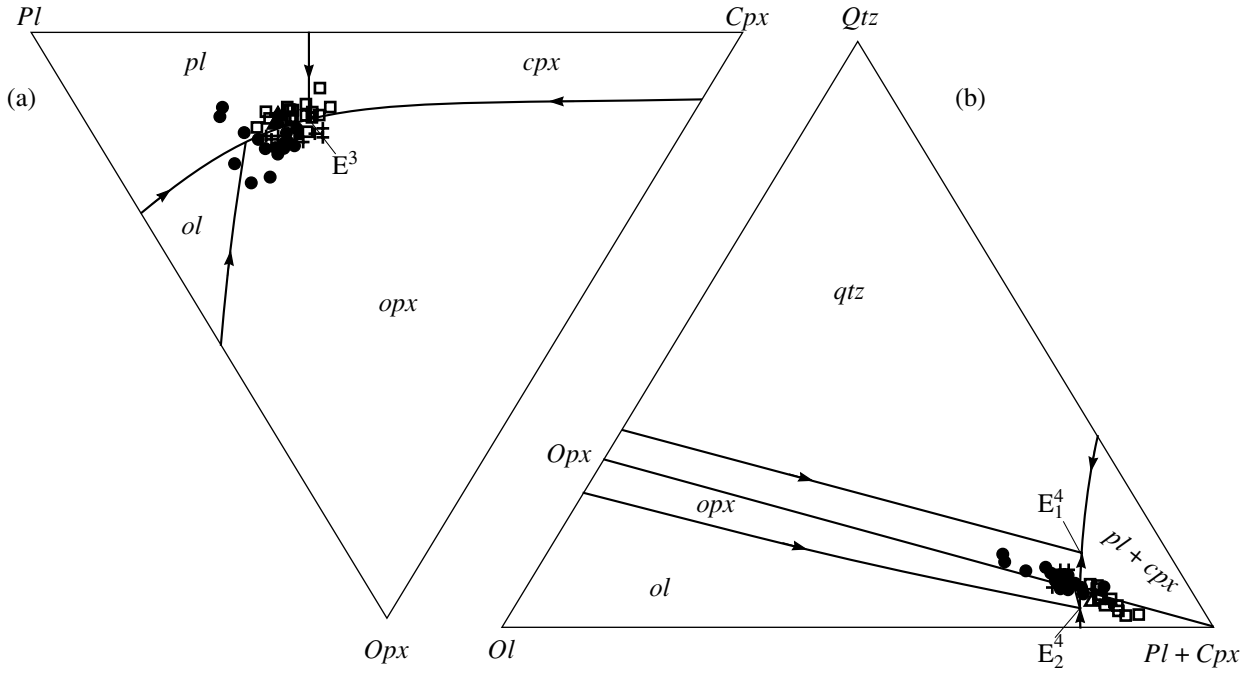


**Fig. 10.** Compositions of the magnetite gabbro and the enclosing rocks on the projections of the isobaric isopleth $Ol^{25–50}$–*Cpx*–$Pl^{60–70}$–*Qtz*–$H_2O$ (Dubrovskii, 1998).

The position of projecting planes relative to the phase diagram is shown in Fig. 8. $E_1^4$ (*Opx* + *Cpx* + *Pl* + *Qtz* = L); $E_2^4$ (*Ol* + *Opx* + *Cpx* + *Pl* = L); $E_3$ (*Opx* + *Cpx* + *Pl* = L). Filled circles are gabbronorites; unfilled triangles, gabbronorites with inverted pigeonite; unfilled squares, magnetite gabbros of the lower belt; and crosses, magnetite gabbros of the upper belt.

Taking the available experimental and natural data on the influence of Fe/(Fe + Mg) ratio of basaltic melt on the pyroxene stability fields (Hess, 1941; Longhi and Pan, 1988; Longhi, 1991), we constructed four schematic isobaric isopleth sections *Opx–Cpx–Pl–Mgt* (+$H_2O$) (Fig. 11) in ascending order of Fe/(Fe + Mg) of the melt. Figure 12 shows the position of these sections on the *T–f* diagram. These isobaric isopleth sections allow us to trace the assumed liquid line of descent for the initial melt. It is evident that the chamber melt *X* should lie on the cotectic line *Opx + Cpx + Pl + L* at the moment of formation of the central part of the intrusion (Fig. 11, $f_1$). The crystallization products of this melt correspond to the *Pl–Cpx–Opx* cumulates, gabbronorites with gabbro and gabbro-ophitic textures composing the main portion of the central part of the intrusion. During crystal fractionation, the Fe/(Fe + Mg) ratio of residual melt increases progressively and the pigeonite volume on the phase diagram expands on the expense of orthopyroxene. Because of this, the melt reaches the point $P_1^4$ at a certain moment of time (Fig. 11, $f_2$). This provided the formation of the *Pl–Cpx–Opx–Pig#* cumulates, gabbronorites with inverted pigeonite, which are characterized by an unusual three-pyroxene assemblage. Finally, the stage of magnetite gabbro (*Pl–Cpx–Opx–Pig#–Mgt* cumulate) formation corresponds to the moment when at increasing Fe/(Fe + Mg) melt reaches the invariant point $T^4$, *Opx + Cpx + Pig + Pl + Mgt* + L and magnetite appears among crystallizing phases (Fig. 11, $f_3$). Theoretically, the subsequent melt evolution should have resulted in orthopyroxene disappearance and replacement by pigeonite (Fig. 11, $f_4$). In our case, this was not observed and the melt terminated its crystallization in the above-mentioned invariant point.

It remains to elucidate the reason of the decrease of pyroxene ratio in the rocks during the above-described crystallization process. Most likely, it is related to the well-known tendency of decreasing *Pl* crystallization volume with increasing albite mole fraction (Bowen, 1915). The essence of this phenomenon is illustrated on the schematic phase diagram of the isopleth *Opx–Cpx–Pl* (Fig. 13), where the decrease in the pyroxene ratio [K(hy)] corresponds to the shift of the "eutectic" $E^3$ from position 1 to 3.

**2. Fine-grained fabric of magnetite gabbro and depletion in incompatible elements.** Among the main unusual features of the magnetite gabbro are its fine-grained textures and depletion in incompatible elements, which are not typical of the residual differentiates of layered massifs. In principle, there is a single mechanism that could be responsible for the formation of fine-grained rocks during chamber melt differentiation. This is rapid melt crystallization caused by sharp supercooling at the elimination of fluid phase from the

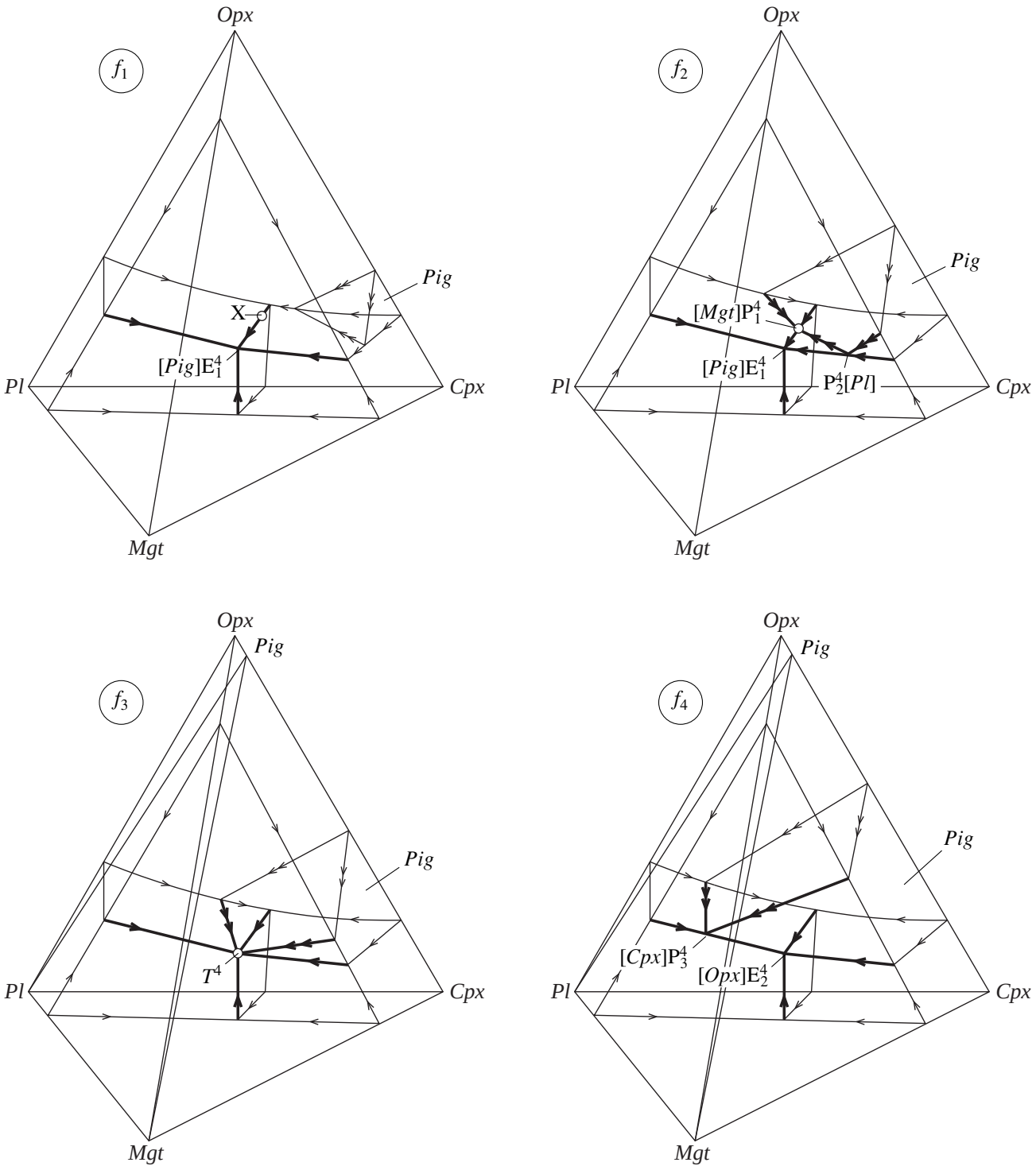


**Fig. 11.** Assumed differentiation trend of the chamber melt of the intrusion on the schematic phase diagrams of the isopleth sections *Opx–Cpx–Pl–Mgt* (+$H_2O$).

$E^4_1$ (*Opx* + *Cpx* + *Pl* + *Mgt* = L); $P^4_1$ (*Opx* + *Cpx* + *Pl* = L + *Pig*); $P^4_2$ (*Opx* + *Cpx* = L + *Pig* + *Mgt*); $P^4_3$ (*Pig* + *Pl* + *Mgt* = L + *Opx*); and $E^4_2$ (*Pig* + *Cpx* + *Pl* + *Mgt* = L). *f* = Fe/(Fe + Mg). X is initial melt. The positions of sections with progressively increasing Fe/(Fe + Mg) of the melt from $f_1$ to $f_4$ are shown in the *T–f* projection (Fig. 12). See text for explanation.

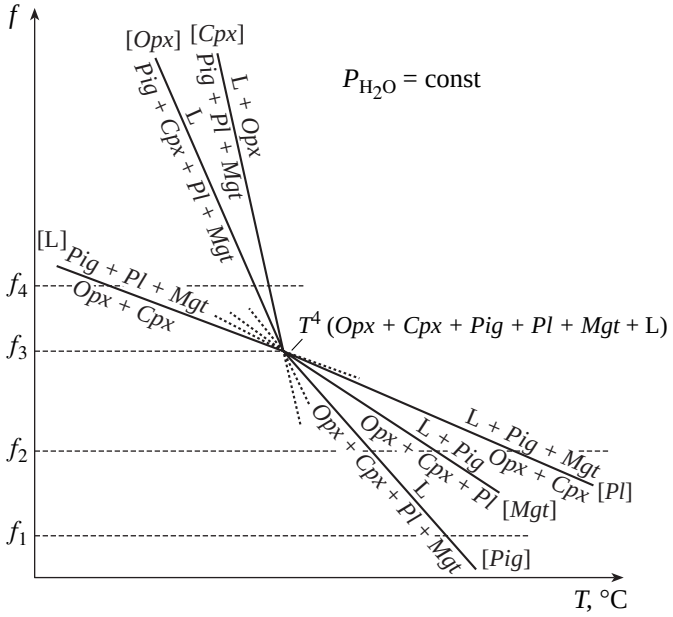


**Fig. 12.** *T–f* projection of the section *Opx–Cpx–Pl–Mgt* ($+H_2O$). *f* = Fe/(Fe + Mg).

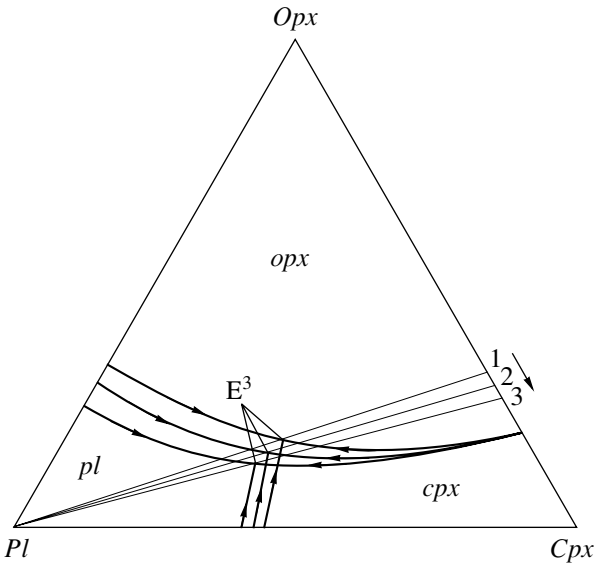


**Fig. 13.** A schematic phase diagram for the isopleth *Opx–Cpx–Pl* ($+H_2O$) showing a decrease in the fraction of *Opx* in the eutectic $E^3$ (*Pl* + *Opx* + *Cpx* = L) with decreasing anorthite mole fraction of normative plagioclase in melt from point 1 to point 3.

system. It is known that, in contrast to lithostatic pressure, fluid pressure significantly reduces liquidus temperature. The difference between "dry" and "hydrous" liquidi may be as high as tens to hundreds of degrees depending on water concentration (Zavaritskii and Sobolev, 1961; Burnham, 1979). As suggested by the eutectic equilibrium *Ol* + *Opx* + *Cpx* + *Pl* = L (Fig. 7), for the initial melt of the Western Pansky Tundra intrusion, the difference between the "dry" and "hydrous" liquidi at a fluid pressure of slightly lower than 1 kbar is about 100°C. This value corresponds to melt supercooling owing to the removal of volatiles from the melt.

Proskuryakov (1967) first invoked the mechanism of degassing (decompression) to explain the fine-grained texture of the magnetite gabbro of the Western Pansky Tundra intrusion. In his opinion, during gabbronorite crystallization, the residual differentiation products were squeezed from the consolidated portions of the intrusion and concentrated in subchambers extending in accord with the general structural plan of the massif. Sometimes, they were subdivided into a series of smaller bodies and their shapes were complicated by bulges and pinches. During crystallization, the opposing walls of the subchambers converged gradually, the volume of liquid decreased and its composition changed, while the fluid pressure increased continuously. Then, instantaneous loss of volatiles was caused by the fracturing of subchamber walls due to tectonic movements and (or) high fluid pressure exceeding the strength of the walls. This brought the melt into a state of strong oversaturation and resulted in its rapid crystallization and formation of fine-grained magnetite gabbro. It should be noted that the occurrence of medium-grained magnetite gabbro in the intrusion suggests that its formation was at least not always accompanied by complete volatiles elimination. The assumption on the controlling role of degassing in the formation of the fine-grained magnetite gabbro bodies is supported by their depletion in incompatible elements, which partition into fluid and must be actively removed from the system with volatiles.

**3. Sharp transition between the magnetite gabbro and enclosing gabbronorite.** Within the concept of the residual nature of the magnetite gabbro, there are two possible explanations for sharp transitions from the magnetite gabbro to the enclosing rocks, which are observed in places. One explanation assumes that residual melt could intrude partially consolidated portions of the intrusion. In such a case, no transitional zone of gabbronorite with inverted pigeonite should probably occur between the magnetite gabbro and enclosing rocks, which is observed in the above-mentioned case. The second explanation is directly related to the proposed decompression mechanism of magnetite gabbro formation. Its essence can be illustrated in a binary diagram with continuous solid solutions, for example in the system *Ab–An* (Fig. 14). During water-saturated fractionation, plagioclase $An_{70}$ crystallizes from the initial melt X (gabbronorite). As fluid pressure decreases at decompression, the composition of residual melt (point X) may be shifted after a short time period under isothermal conditions from the liquidus region (1) through subliquidus (2) into the subsolidus region (3). In accord with the topology of the phase diagram, the composition of crystallizing plagioclase should change abruptly toward the low-temperature members of solid

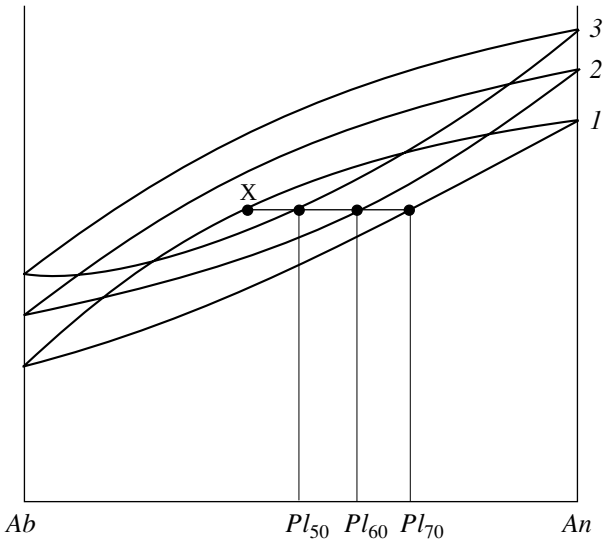


**Fig. 14.** Binary phase diagram of continuous solid solutions *Ab–An* showing the influence of isothermal polybaric crystallization on plagioclase composition.

X is the point of melt composition. *1* and *3* are the positions of liquidus and solidus lines before and after the extraction of fluid from the system, and *2* is some intermediate state. See text for explanation.

solution: from $An_{70}$ to $An_{60}$ and $An_{50}$ (magnetite gabbro). Such a crystallization path corresponds to the definition of the isothermal polybaric crystallization of silicate melt. In contrast to a more common case of crystallization at decreasing temperature, it occurs at decreasing pressure at constant temperature (Tuttle and Bowen, 1958).

**4. Simultaneous occurrence of residual differentiates with different mineral compositions (olivine-bearing and olivine-free) in the intrusion.** Perhaps, one of the most complicated problem is that of the appearance of olivine-bearing gabbro enclosed by olivine-free gabbronorite in the upper layer. The phase diagram of the isopleth *Ol–Cpx–Pl–Qtz* (+$H_2O$) (Fig. 8, left inset) indicates that this variety of magnetite gabbro should correspond to the differentiation trend from the eutectic $E^3$, *Opx* + *Cpx* + *Pl* + L to the eutectic $E_2^4$, *Ol* + *Opx* + *Cpx* + *Pl* + L. The poikilitic character of olivine grains suggests that the melt reached the eutectic $E_2^4$, where olivine joined the crystallizing phases, only at the period of intercumulus liquid crystallization.

The problem is thus reduced to distinguishing the reason of the shift of initial melt composition from the boundary isopleth *Opx–Cpx–Pl* (+$H_2O$) into the volume of olivine-normative isopleth. Additional investigations are required to resolve the dilemma. As a working hypothesis, it can be supposed that the change in residual melt composition was the removal of a certain amount of $SiO_2$ with fluid phase during degassing. Experimental results demonstrate that supercritical water vapor (fluid) can actively dissolve and transport $SiO_2$ (Gillinham, 1950). These data do not contradict such a possibility.

## CONCLUSION

Physicochemical analysis allowed us to accept the hypothesis of magnetite gabbro formation from the residual melt of the Western Pansky Tundra intrusion as the most feasible. The phase, modal, and cryptic layering near the bodies of magnetite gabbro finds its explanation within such a model and can be correlated with the trend of chamber fractionation of the intrusion according to the schematic phase diagrams of isopleth sections *Opx–Cpx–Pl–Mgt* (+$H_2O$). A number of observations that seem to contradict this model are related to the complication of the theoretical differentiation trend of initial melt under the influence of various factors. The most important among them are the loss of fluid phase enriched in incompatible elements at the final stage of crystallization; crystallization of residual melt under isothermal polybaric conditions owing to decompression; change in melt composition due to degassing; and injection of residual melt into consolidated portions of the intrusion. In our opinion, these deviations from the general scheme of formation of the final differentiation products of layered massifs resulted in a variety of hypotheses on the genesis of these unusual objects in the Western Pansky Tundra intrusion. Further development of the proposed model of magnetite gabbro formation should include the construction of a general physical model for the explanation of mechanisms of residual melt localization at three stratigraphic levels in the central part of the intrusion.

## ACKNOWLEDGMENTS

The authors are grateful to F.P. Mitrofanov for the discussion of an earlier variant of the manuscript, M.I. Dubrovskii for constructive criticism and interest to our work, and our colleagues N.L. Balabonin, Zh.A. Fedotov, and V.I. Skiba (Geological Institute, Kola Research Center, Russian Academy of Sciences) for a number of helpful comments to the text of the paper. The final variant of the manuscript was significantly improved owing to reviews by R.A. Ishbulatov (Institute of Experimental Mineralogy, Russian Academy of Sciences), A.A. Ariskin (Vernadsky Institute of Geochemistry and Analytical Chemistry, Russian Academy of Sciences), and L.L. Perchuk (Moscow State University), whom we express our kind appreciation. The work was financially supported by the grant of the Thule Institute, Oulu University (to R.M. Latypov).

## REFERENCES


Abzalov, M.Z., Veselovskii, N.N., Korchagin, A.U., *et al.*, Silver Minerals in the Layered Plutonic Complex of the Fedorovo–Pansky Tundra, Kola Peninsula, *Dokl. Akad. Nauk*, 1993, vol. 329, no. 4, pp. 497–499.

Alapieti, T.T., Filen, B.A., and Lahtinen, J.J., Proterozoic Layered Intrusions in the Northeastern Part of the Fennoscandian Shield, *Mineral. Petrol.*, 1990, vol. 42, pp. 1–22.

Amelin, Yu.V., Heaman, L.M., and Semenov, V.S., U–Pb Geochronology of Layered Mafic Intrusions in the Eastern Baltic Shield: Implications for the Timing and Duration of Paleoproterozoic Continental Rifting, *Precambrian Res.*, 1995, vol. 75, pp. 31–46.

Ashwal, L.D., *Anorthosites*, Berlin: Springer, 1993.

Balabonin, N.N., Korchagin, A.U., Latypov, R.M., and Subbotin, V.V., Fedorovo–Pansky Intrusion, *Kola Belt of Layered Intrusions. Guide to Pre-Symposium Field Trip VII Intern. Platinum Symp.*, Mitrofanov, F. and Torokhov, M., Eds., Apatity, 1994, pp. 9–41.

Balashov, Y.A., Bayanova, T.B., and Mitrofanov, F.P., Isotope Data on the Age and Genesis of Layered Basic–Ultrabasic Intrusions in the Kola Peninsula and Northern Karelia, Northeastern Baltic Shield, *Precambrian Res.*, 1993, vol. 64, pp. 197–205.

Batieva, I.D., *Petrologiya shchelochnykh granitov Kol'skogo poluostrova* (Petrology of Peralkaline Granites of the Kola Peninsula), Leningrad: Nauka, 1976.

Bayanova, T.B., Levkovich, N.V., and Ivanova, L.V., Zircon–Baddeleyite Geochronological System in the Precambrian Rocks of the Kola Region, in *Materialy devyatoi molodezhnoi nauchnoi konferentsii Geologiya Baltiiskogo shchita i drugikh dokembriiskikh oblastei Rossii* (Proc. 9th Youth Sci. Conf. Geology of the Baltic Shield and other Precambrian Regions of Russia), Apatity, 1995, pp. 25–33.

Bayanova, T.B., Mitrfoanov, F.P., Korchagin, A.U., and Pavlichenko, L.V., Age of Gabbronorite from the Lower Layered Horizon (Reef) of the Fedorovo–Pansky Massif (Kola Peninsula), *Dokl. Akad. Nauk*, 1994, vol. 337, no. 1, pp. 95–97.

Borisova, V.V., Dubrovskii, M.I., Karpov, S.M., *et al.*, Petrology of the Pansky Layered Massif (Kola Peninsula): Paragenetic Analysis, *Zap. Vseross. Mineral. O–va*, 1999, no. 3, pp. 31–48.

Bowen, N.L., The Crystallization of Haplobasaltic, Haplodioritic and Related Magmas, *Am. J. Sci.*, 1915, Ser. 4, vol. 236, pp. 161–185.

Bowen, N.L. and Schairer, I.F., The System MgO–FeO–$SiO_2$, *Am. J. Sci.*, 1935, vol. 22, pp. 345–350.

Boyd, F.R. and Schairer, J.F., The System $MgSiO_3$–$CaMgSi_2O_6$, *J. Petrol.*, 1964, vol. 6, pp. 275–309.

Burnham, C.W., The Importance of Volatile Constituents, *The Evolution of the Igneous Rocks*, Joder, H.S., Jr., Ed., Princeton: Princeton Univ., 1979, pp. 439–482.

Cann, J.R., Upward Movement of Granitic Magma, *Geol. Mag.*, 1970, vol. 107, no. 4, pp. 335–430.

Condliffe, E., Melting Relationships of Selected Rocks of Dioritic Mineralogy, *Progr. Experim. Petrol.*, 1976, vol. 3, pp. 54–55.

Dixon, J.E., Stolper, E.M., and Holloway, J.R., An Experimental Study of Water and Carbon Dioxide Solubilities in Mid-Ocean Ridge Basaltic Liquids. Part I: Calibration and Solubility Models, *J. Petrol.*, 1995, vol. 36, pp. 1607–1631.

Dokuchaeva, V.S., Petrology and Conditions of Ore Mineralization in the Fedorovo–Pansky Intrusion, in *Geologiya i genezis mestorozhdenii platinovykh metallov* (Geology and Genesis of Platinum-Group Metal Deposits), Moscow: Nauka, 1994, pp. 87–100.

Dubrovskii, M.I., *Fiziko-khimicheskie ($P_{H_2O}$–T–X) modeli kristallizatsii magmaticheskikh olivinnormativnykh porod normal'noi shchelochnosti* [Physicochemical ($P_{H_2O}$–T–X) Models of Crystallization of Olivine-Normative Rock of Normal Alkalinity], St. Petersburg: Nauka, 1993.

Dubrovskii, M.I., *Trendy differentsiatsii olivinnormativnykh bazitovykh i ul'trabazitovykh magm normal'noi shchelochnosti i sootvetstvuyushchie im porodnye serii* (Differentiation Trends of Olivine-Normative Basic and Ultrabasic Magmas of Normal Alkalinity and Respective Rock Series), Apatity: Kol'sk. Nauchn. Tsentr Ross. Akad. Nauk, 1998.

Eales, H.V. and Cawthorn, R.G., The Bushveld Complex, *Layered Intrusions*, Cawthorn, R.G., Ed., *Developments in Petrology*, 1996, vol. 15, pp. 181–229.

Fyfe, W.S., Some Thoughts on Granitic Magmas, *Mechanism of Igneous Intrusion*, Newall, G. and Rast, N., Eds., Liverpool: Gallery, 1970, pp. 201–216.

Gillinham, T.E., Solubility and Transport of Silica and Other Nonvolatiles by Water Vapor, in *Voprosy fiziko-khimii v mineralogii i petrografii* (Physicochemical Problems in Mineralogy and Petrography), Moscow: Inostr. Literatura, 1950, pp. 77–112.

Gruenewaldt, G., On the Phase Change Orthopyroxene–Pigeonite and the Resulting Texture in the Main and Upper Zone of the Bushveld Complex in the Eastern Transvaal, *Geol. Soc. S. Afr., Spec. Publ.*, 1970, vol. 1, pp. 67–73.

Hamilton, D.L., Burnham, C.W., and Osborn, E.F., The Solubility of Water and Effects of Oxygen Fugacity and Water Content on Crystallization in Mafic Magmas, *J. Petrol.*, 1964, vol. 5, pp. 21–39.

Hanski, E.J., Petrology of the Pechenga Ferropicrites and Cogenetic, Ni-bearing Gabbro–Wehrlite Intrusions at Pechenga, Kola Peninsula, Russia, *Acad. Dissertation, Geol. Surv. Finl. Bull.*, 1992, vol. 367.

Hess, H.H., Pyroxenes of Common Mafic Magmas. Part 2, *Am. Mineral.*, 1941, vol. 26, pp. 573–594.

*Imandra–Varzugskaya zona karelid* (Imandra–Varzuga Karelide Zone), Gorbunov, G.I., Ed., Leningrad: Nauka, 1982.

Johnson, M.C., Anderson, A.T., Jr., and Rutherford, M.J., Pre-Eruptive Volatile Contents of Magmas, *Volatiles in Magmas*, Carroll, M.R. and Holloway, J.R., Eds., *Rev. Mineral.*, 1994, vol. 30, pp. 281–330.

Kadik, A.A., Lebedev, E.V., and Khitarov, N.I., *Voda v magmaticheskikh rasplavakh* (Water in Igneous Melts), Moscow: Nauka, 1971.

Korchagin, A.U., Bakushkin, E.M., Vinogradov, L.A., *et al.*, Geologic Structure of the Lower Boundary Zone of the Pansky Tundra Massif and Its Platinum-Group Mineralization, in *Geologiya i genezis mestorozhdenii platinovykh metalov* (Geology and Genesis of Platinum-Group Metal Deposits), Moscow: Nauka, 1994, pp. 100–106.

Korzhinskii, D.S., *Fiziko-khimicheskie osnovy analiza paragenezisov mineralov* (Physicochemical Basis for the Analysis of Mineral Parageneses), Moscow: Akad. Nauk SSSR, 1957.

Korzhinskii, D.S., *Teoreticheskie osnovy analiza paragenezisov mineralov* (Theoretical Basis for the Analysis of Mineral Parageneses), Moscow: Nauka, 1973.

Kozlov, E.K., *Estestvennye ryady porod nikelenosnykh intruzii i ikh metallogeniya* (Intrinsic Rock Series of Nickel-bearing Intrusions and Their Metallogeny), Leningrad: Nauka, 1973.

Latypov, R.M., Nature of Rhythmic Layering in the Pansky Tundra Intrusion, Kola Peninsula, *Dokl. Akad. Nauk*, 1994, vol. 336, no. 5, pp. 643–647.

Latypov, R.M., Origin of Anorthosite in the Layered Intrusion of the Pansky Tundra: Geological Data (Kola Peninsula), *Geol. Geofiz.*, 1995, vol. 36, no. 3, pp. 55–63.

Latypov, R.M., Mitrofanov, F.P., Alapieti, T.T., and Halkoaho, T.A., Petrology of the Lower Layered Horizon of the Western Pansky Tundra Intrusion, Kola Peninsula, *Petrologiya*, 1999, vol. 7, no. 5, pp. 509–538.

Longhi, J., Comparative Liquidus Equilibria of Hypersthene-Normative Basalts at Low Pressure, *Am. Mineral.*, 1991, vol. 76, pp. 785–800.

Longhi, J. and Pan, V., A Reconnaissance Study of Phase Boundaries in Low-Alkali Basaltic Liquids, *J. Petrol.*, 1988, vol. 29, pp. 115–147.

Mitrofanov, F.P., Yakovlev, Yu.N., Distler, V.V., *et al.*, Kola Region—A New Platinum Metal Province, in *Geologiya i genezis mestorozhdenii platinovykh metallov* (Geology and Genesis of Platinum-Group Metal Deposits), Moscow: Nauka, 1994, pp. 65–79.

Odinets, A.Yu., Petrology of the Pansky Massif of Mafic Rocks (Kola Peninsula), *Cand. Sc. (Geol.–Min.) Dissertation*, Leningrad: Leningrad Univ., 1971.

Proskuryakov, V.V., Geologic Structure and Differentiation Character of the Mafic Intrusion of the Pansky Hills, Kola Peninsula, in *Osnovnye i ul'traosnovnye porody Kol'skogo poluostrova* (Basic and Ultrabasic Rocks of the Kola Peninsula), Leningrad: Nauka, 1967, pp. 40–54.

Rundkvist, T.V., *Pozdne- i postmagmaticheskoe mineraloobrazovanie v Panskom massive (Kol'skii poluostrov)* (Late and Postmagmatic Mineralization in the Pansky Massif, Kola Peninsula), Apatity: Poligraf, 1999.

Sobolev, A.V., Problems of Formations and Evolution of Mantle Magmas, *Doctoral (Geol.–Min.) Dissertation*, Moscow: Vernadsky Inst. Geochem. Anal. Chem., 1997.

Spulber, S.D. and Rutherford, M.J., The Origin of Rhyolite and Plagiogranite in Oceanic Crust: An Experimental Study, *J. Petrol.*, 1983, vol. 24, pp. 1–25.

Tuttle, O.F. and Bowen, N.L., Origin of Granite in the Light of Experimental Studies in the System $NaAlSi_3O_8$–$KAlSi_3O_8$–$SiO_2$–$H_2O$, *Geol. Soc. Am. Mem.*, 1958, vol. 74.

Yoder, H.S. and Tilley, C.E., Origin of Basalt Magmas: An Experimental Study of Natural and Synthetic Rock Systems, *J. Petrol.*, 1962, vol. 3, pp. 342–532.

Zavaritskii, A.N. and Sobolev, V.S., *Fiziko-khimicheskie osnovy petrografii izverzhennykh porod* (Physicochemical Basis of the Petrography of Igneous Rocks), Moscow: Gosgeoltekhizdat, 1961.

Zharikov, V.A., *Osnovy fiziko-khimicheskoi petrologii* (Principles of Physicochemical Petrology), Moscow: Mosk. Gos. Univ., 1976.